# High-harmonic generation in solids

#### Lisa Ortmann and Alexandra S. Landsman\*

Department of Physics, The Ohio State University, Columbus, OH, United States \*Corresponding author: e-mail address: landsman.7@osu.edu

#### Contents

1.	Intro	oduction	104
2.	Understanding HHG in solids		105
	2.1	Interband polarization and intraband currents: An introduction	105
	2.2	Intraband mechanism of HHG	108
	2.3	Details on the interband mechanism	114
	2.4	Theoretical methods	117
	2.5	The role of the dephasing time	121
	2.6	The cutoff	124
	2.7	Intraband versus interband	125
	2.8	Comparison of HHG in gases and solids	131
3.	Applying HHG in solids		135
	3.1	Reconstructing the band structure (in reciprocal space)	135
	3.2	Reconstructing the crystal lattice (in real space)	136
	3.3	Symmetry effects	136
	3.4	Measuring the Berry curvature	138
	3.5	Extracting higher order nonlinear susceptibilities	141
	3.6	Controlling HHG in solids via doping	142
	3.7	HHG in graphene and other 2D materials	142
4.	Cor	nclusion and outlook	144
Acknowledgments			146
References			146

#### **Abstract**

The last decade saw attosecond physics, traditionally focused on atomic and molecular gases, move rapidly into the condensed matter phase. This expansion was stimulated by experimental observation of high-harmonic generation (HHG) from solids. HHG, first observed in atomic gas a few decades ago, is a unique process underlying the creation of attosecond pulses and has many other applications involving imaging and controlling electron dynamics. Although insights from strong field atomic physics were instrumental to our understanding of HHG in solids, the unique properties of crystalline structure lead to a rich variety of new phenomena unique to solids. This has resulted

in a rapid expansion of the field, as is evidenced by the growing body of research at the intersection of attosecond physics and condensed matter. Here, we review some notable advances over the past decade, highlighting open questions and some recent developments.

# 1. Introduction

Over the past twenty years, the field of ultrafast laser physics has become a significant force not only in atomic, molecular, and optical physics but also at the interface of multiple areas of fundamental and applied science that involve imaging and control of electron dynamics. Its progress was enabled by the creation of high-intensity, ultrashort optical pulses—a technological breakthrough recognized with a Nobel Prize in Physics in 2018. These pulses carry sufficient intensity to ionize a sample, even though the photon frequency is much below the ionization potential. Yet, they last only a few femtoseconds, ensuring that there is little material damage. From a fundamental physics viewpoint, this presents a unique opportunity to observe in real time the highly nonlinear and nonperturbative electronic response of matter to intense radiation.

While the technology behind these intense ultrashort optical pulses was developed in the 1980s, the theory describing their interaction with matter came about earlier. It started with the seminal work of Keldysh, who developed a theoretical framework to understand ionization of matter by intense low-frequency fields (Keldysh, 1965). The Keldysh parameter in atomic units,  $\gamma = \omega \sqrt{2I_v}/F$ , where  $\omega$ ,  $I_v$ , and F are the frequency, ionization potential, and peak laser field strength (respectively), is commonly used to describe strong field ionization. In particular,  $\gamma \gg 1$  corresponds to multiphoton ionization, and  $\gamma \ll 1$  corresponds to the adiabatic tunneling limit, with typical experiments using infrared radiation falling in the  $\gamma \sim 1$ range. The underlying theory, known as the strong field approximation (SFA), which has since been developed and refined by others (Faisal, 1973; Perelomov et al., 1966; Reiss, 1980), is fundamental to our understanding of the phenomena resulting from strong field excitations. This famously includes the process of high-harmonic generation (HHG), which underlies the creation of attosecond pulses (Lewenstein et al., 1994). HHG can be described as follows: a strong laser field bends the binding potential of the atom, causing the valence electron to tunnel out. This electron is subsequently accelerated in the continuum and, when the laser field reverses direction, recombines with the parent atom, emitting a harmonic that is a

multiple of the driving laser frequency (Corkum, 1993; Schafer et al., 1993). The study of HHG and many other strong field processes has been the province of attosecond physics (Krausz and Ivanov, 2009).

In his original work that established the strong field approximation (SFA), Keldysh treated solids and atoms on equal footing (Keldysh, 1965). Yet, over the decades that followed, the two fields have diverged and the application of the theory that Keldysh pioneering was largely confined to atomic gas. The field, stimulated by the first observation of HHG in solids in 2011 (Ghimire et al., 2011), has now come full circle, with attosecond physics increasingly turning its attention to condensed matter systems.

Here, we review high-harmonic generation in solids coming from this perspective, which extends well-established insights from strong field atomic physics to condensed matter. At the same time, the periodic nature and the accompanying band structure of the crystalline solid lead to a number of rich phenomena that are entirely absent in atomic gas. Notably, the nonparabolic nature of the conduction bands results in high harmonics generated by dynamic Bloch oscillations (otherwise known as the intraband mechanism)—a phenomenon absent in atomic gas. Hence, Section 2 focuses on the different mechanisms of HHG in solids, highlighting their commonality and differences with HHG in isolated atoms. In Section 3, we turn our attention to the many applications of HHG in solids. Our aim is not to give a comprehensive account of all significant developments, which is beyond the scope of this review. Rather, we attempt to highlight some of the notable advances in this rapidly growing and evolving field. In the conclusion, we touch on a few other important topics not treated in this review, such as HHG from plasmonically enhanced fields in the vicinity of nanostructures and correlation effects.

# 2. Understanding HHG in solids

This section provides an in-depth introduction to high-harmonic generation (HHG) in solids. We will focus on the mechanisms used to describe HHG in solids and discuss related properties such as the cutoff of the harmonic spectra or the role of the dephasing time.

# 2.1 Interband polarization and intraband currents: An introduction

There are two main mechanisms leading to HHG in solids that are usually considered. The first one is interband polarization, which has much in common with the three-step model used to explain HHG in the gas phase

(Corkum, 1993; Lewenstein et al., 1994; Schafer et al., 1993). In the gas phase, interaction with a strong and short laser pulse leads to an electron tunneling out of the atom or molecule into the continuum (step 1) where it is accelerated by the incident laser field (step 2). Some of these electrons will return to their parent ion and recombine, emitting a photon of frequency  $\omega$ , corresponding to the energy  $\Delta E = \hbar \omega$  released in the recombination process (step 3).

Similarly, interaction of a strong and short laser pulse with a solid can result in tunneling of electrons from the valence into the conduction band (step 1, see Fig. 1D for an illustration). The electron in the conduction band and the corresponding hole in the valence band are accelerated by the driving laser field (step 2). Upon recombination of the electron with its hole in the valence band, light is emitted at a frequency  $\omega$  corresponding to the energy difference  $\Delta E = \hbar \omega$  between the valence and the conduction band at the position in k-space where the electron was found at the time of recombination (step 3) (Vampa et al., 2014). This mechanism is called the interband mechanism, with the prefix "inter" highlighting the transition between the conduction and valence band in the recombination step.

Another mechanism often used to explain HHG in solids is the intraband current (Ghimire et al., 2011; Luu et al., 2015). Here, we need again the transition of an electron from the valence to the conduction band, realized by interaction with the laser pulse. The electron is driven by the laser field in the anharmonic conduction band. Likewise, the hole is driven in the anharmonic valence band by the laser. The anharmonicity of the conduction and valence band can be described by higher order cosine terms, as also illustrated in Fig. 1B. The strongly anharmonic motion of the electrons (and holes) leads to an overall anharmonic current that results in emission of higher order harmonic light. Since the currents responsible for the light emission are found within separate bands, with the electron in the conduction band and the hole in the valence band, this is called the intraband mechanism.

Thus, we have two mechanisms that, in principle, are able to explain the generation of high harmonic light from a solid. But which one is the one we should use to describe the HHG light observed in experiments? Or which mechanism dominates in a particular experiment? These questions have been discussed extensively in the past decade and the dispute is not settled yet. We will review the different positions and arguments of this debate in Section 2.7. Before getting there, however, we will explain the interband and intraband mechanisms in greater detail.

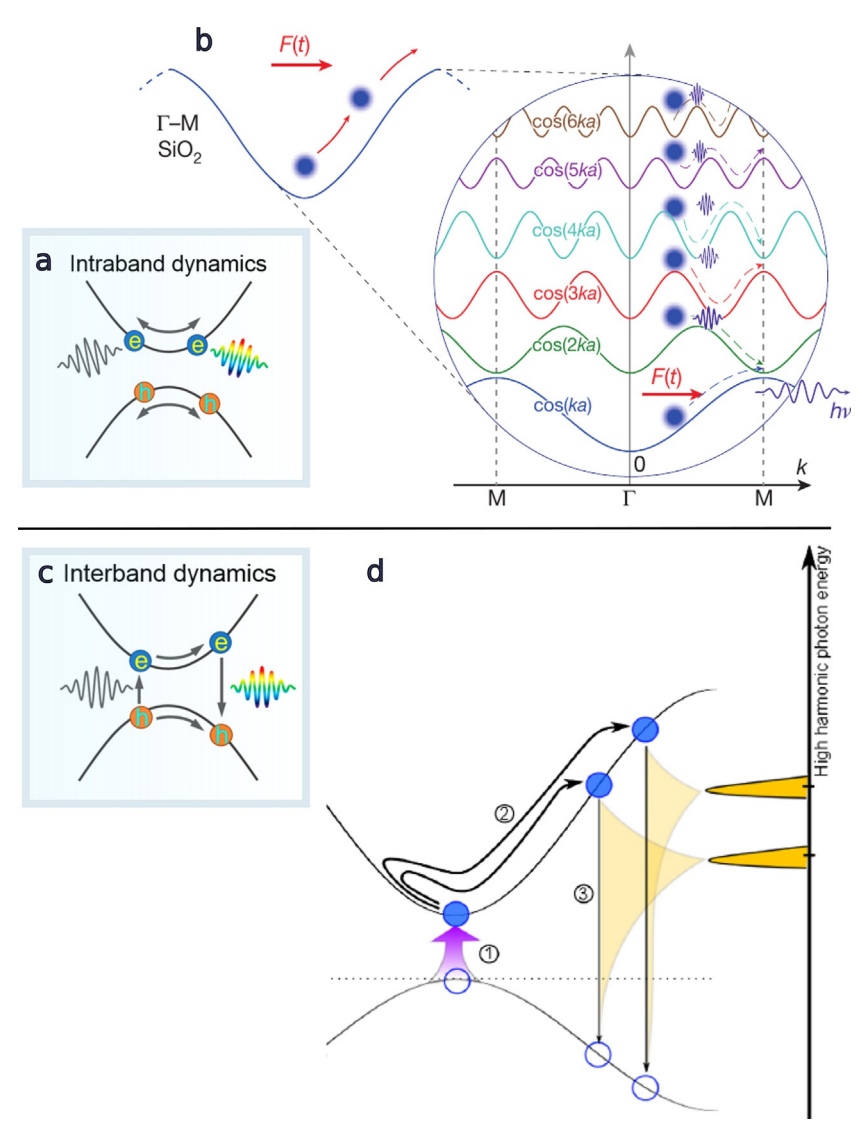


**Fig. 1** Illustration of intraband (A,B) and interband (C,D) mechanism. Panel (B) illustrates details of the intraband mechanism. After the electrons have been promoted from the valence into the conduction band, the laser drives the electron in the anharmonic band structure of the conduction band, illustrated by higher order cosine terms. This results in an anharmonic electron current that emits high harmonic light. Similarly, the hole is driven in the anharmonic band structure of the valence band and can emit high harmonic light. Panel (D) illustrates details of the interband mechanism. The electron tunnels from the valence into the conduction band (step 1) are accelerated in the conduction band (step 2) and recombine with the corresponding hole in the valence band. High harmonic light is emitted with a photon energy that equals the band gap energy at (Continued)

#### 2.2 Intraband mechanism of HHG

Here, we present a semiclassical single electron picture of the intraband mechanism, which will provide an intuitive and simple model. A more elaborate and numerically involved but less intuitive model for the intraband mechanism will be presented later in Section 2.4.

#### 2.2.1 Equations of motion in a periodic lattice

In this subsection, we derive the equations of motions of an electron in a solid, following the description in Hofmann (2015). The result will be used in the next subsection to derive the intraband current and its light emission.

We treat the electron as a wave packet, a superposition of many Bloch waves with different values of the crystal momentum k, that has a group velocity

$$\nu_g = \frac{\mathrm{d}\omega(k)}{\mathrm{d}k} = \frac{1}{\hbar} \frac{\mathrm{d}\mathcal{E}(k)}{\mathrm{d}k},\tag{1}$$

where  $\mathcal{E}(k) = \hbar \omega(k)$  defines the dispersion relation of the band structure. Now, if a particle with charge -e and group velocity  $\nu_g$  is exposed to an electric field F, then within the infinitesimally short time dt its energy will change by

$$d\mathcal{E} = -eF\nu_{g}dt. \tag{2}$$

Replacing  $v_g$  by the definition in Eq. (1) and using

$$\frac{\mathrm{d}\mathcal{E}}{\mathrm{d}t} = \frac{\mathrm{d}\mathcal{E}}{\mathrm{d}k} \frac{\mathrm{d}k}{\mathrm{d}t} \tag{3}$$

**Fig. 1—cont'd** the point of recombination (step 3). Panels (A) and (C): Reprinted (adapted) with permission from Nishidome, H., Nagai, K., Uchida, K., Ichinose, Y., Yomogida, Y., Miyata, Y., Tanaka, K., Yanagi, K., 2020. Control of high-harmonic generation by tuning the electronic structure and carrier injection. Nano Lett. 20 (8), 6215–6221. Copyright 2020 American Chemical Society. Panel (B): Reprinted by permission from Springer Nature Customer Service Centre GmbH: Springer; Luu, T. T., Garg, M., Kruchinin, S. Y., Moulet, A., Hassan, M. T., Goulielmakis, E., 2015. Extreme ultraviolet high-harmonic spectroscopy of solids. Nature 521 (7553), 498–502. Copyright 2015. Panel (D): Reprinted figure with permission from Vampa, G., Hammond, T. J., Thiré, N., Schmidt, B. E., Légaré, F., McDonald, C. R., Brabec, T., Klug, D. D., Corkum, P. B., 2015a. All-optical reconstruction of crystal band structure. Phys. Rev. Lett. 115 (19), 193603. Copyright 2015 by the American Physical Society.

leads to

$$\hbar \frac{\mathrm{d}k}{\mathrm{d}t} = -eF. \tag{4}$$

One may think that if we set  $p = \hbar k$ , then this looks just like the equation describing an electron in free space (i.e., not in a lattice) that is exposed to an electric field F. However, it is important to note that  $\hbar k$  is not the momentum of Bloch electrons (Hofmann, 2015) but their crystal momentum and the interpretation of Eq. (4) should rather be as follows: The electric field causes the Bloch electrons to change their crystal momentum k, and the rate of change is given by the external force (here: the field strength) (Hofmann, 2015) and not the total force that would include the periodic field of the crystal lattice. The change of a free electron's momentum, in contrast, is proportional to the total force (Ashcroft et al., 1976).

Using the above equations, the acceleration can be obtained as follows:

$$a = -\frac{\mathrm{d}\nu_g}{\mathrm{d}t} = \frac{1}{\hbar} \frac{\mathrm{d}}{\mathrm{d}t} \frac{\mathrm{d}\mathcal{E}(k)}{\mathrm{d}k} = \frac{1}{\hbar} \frac{\mathrm{d}^2 \mathcal{E}(k)}{\mathrm{d}k^2} \frac{\mathrm{d}k}{\mathrm{d}t} = -\frac{1}{\hbar^2} \frac{\mathrm{d}^2 \mathcal{E}(k)}{\mathrm{d}k^2} eF. \tag{5}$$

The rightmost expression looks like Newton's equation for a particle with mass  $d^2\mathcal{E}(k)/dk^2$ . Therefore, this second-order derivative of the band structure with respect to k is often called the effective mass of the particle moving in the crystal (Hofmann, 2015).

#### 2.2.2 Derivation of the intraband current

As the intraband contribution to the high harmonic radiation is due to the anharmonic movement of the electron and hole in their respective bands, we will assume that the transition from the valence to the conduction band has already happened and the electron in the conduction band and the hole in the valence band are ready to be driven by the electric field (see Fig. 1A). Quantifying the transition rate is of relevance, though, if one wants to know how many carriers are available for acceleration in the bands.

In the following, we will focus on the motion of the electron in the conduction band. Note, though, that the same arguments apply to holes in the valence band. Sometimes, the intraband current due to hole motion in the valence band is omitted entirely in the literature, since holes often contribute less to the harmonic generation due to a larger effective mass (Ghimire et al., 2012a).

For the description of the electron motion driven by an electric field in the conduction band we will use Eq. (4). Applying atomic units ( $e = \hbar = m_e = 1$ ) and assuming an electric field oscillating with frequency  $\omega_0$  under a constant envelope

$$F(t) = F_0 \cos(\omega_0 t), \tag{6}$$

Eq. (4) becomes

$$\frac{\mathrm{d}k(t)}{\mathrm{d}t} = -F(t) = -F_0 \cos(\omega_0 t) \tag{7}$$

and integration with respect to time gives

$$k(t) = -\int_0^t F(t') dt' = -\int_0^t F_0 \cos(\omega_0 t') dt' = -\frac{F_0}{\omega_0} \sin(\omega_0 t).$$
 (8)

We will expand the band structure into a series of higher order cosine terms

$$\mathcal{E}(k) = \sum_{l=0}^{\infty} c_l \cos(jka), \tag{9}$$

which is also illustrated in Fig. 1B. Here, a is the lattice constant and in practice the coefficients  $c_l$  may be obtained by fitting Eq. (9) to the band structure of the crystal. To this end, one may reduce the number of orders included in the fit. The highest order included,  $l_{max}$ , can be related to the highest characteristic distance  $l_{max}a$  in the crystal (Luu et al., 2015). Substituting Eqs. (9) and (8) into Eq. (1), we obtain

$$\nu_{g}(t) = \frac{\mathrm{d}\mathcal{E}(k)}{\mathrm{d}k} = -\sum_{l=1}^{l_{max}} lac_{l}\sin\left(lak(t)\right)$$

$$= -\sum_{l=1}^{l_{max}} lac_{l}\sin\left(-la\frac{F_{0}}{\omega_{0}}\sin\left(\omega_{0}t\right)\right)$$

$$= \sum_{l=1}^{l_{max}} lac_{l}\sum_{n=1} J_{2n-1}\left(\frac{laF_{0}}{\omega_{0}}\right)\sin\left((2n-1)\omega_{0}t\right),$$
(10)

where in the last step the Jacobi-Anger expansion was used to rewrite the "sine of a sine" in terms of Bessel functions  $J_m$  of first kind of order m (Golde et al., 2008). The current can be obtained from the group velocity as

$$j(t) = -\frac{2e}{(2\pi)^3} \int_{BZ} \nu_g(k, t) f_g(k, t) d^3k$$
 (11)

with  $f_g(k, t)$  being the time-dependent distribution function of the wave packet, e.g., a Gaussian wave packet (Feise and Citrin, 1999 and SI of Luu et al., 2015). For the sake of simplicity and analytical tractability, we will consider here a wave packet that is localized at one k and does not spread (Kaneshima et al., 2018; Luu et al., 2015), which reduces the current to be proportional to the group velocity

$$j(t) \propto \nu_{\sigma}(t).$$
 (12)

Therefore, instead of calculating the high harmonic yield  $I_{HHG}$  from the time derivative of the current (Mücke, 2011),

$$I_{HHG}(t) \propto \left| \frac{\partial j(t)}{\partial t} \right|^2 \xrightarrow{\text{FFT}} I_{HHG}(\omega) \propto \left| \omega \tilde{j}(\omega) \right|^2,$$
 (13)

we can directly use the time derivative of the group velocity

$$I_{HHG}(t) \propto \left| \frac{\partial v_g(t)}{\partial t} \right|^2 \xrightarrow{\text{FFT}} I_{HHG}(\omega) \propto \left| \omega \tilde{v}_g(\omega) \right|^2.$$
 (14)

Thus, applying Eq. (14) to Eq. (10), we obtain for the Nth harmonic with N = (2n - 1), where  $n \in \mathbb{N} > 0$ 

$$I_{HHG,N}(\omega) \propto \left| N\omega_0 \sum_{l=1}^{l_{max}} lac_l J_N \left( \frac{laF_0}{\omega_0} \right) \right|^2,$$
 (15)

where we used

$$FT\{\sin((2n-1)\omega_0 t)\} \propto \delta(\omega - (2n-1)\omega_0). \tag{16}$$

Let us briefly consider how the above calculation would have looked had we assumed a parabolic band structure  $E(k) \propto k^2$ , corresponding to motion of the electron in free space. Then, we would have  $v_g \propto k(t) \propto \sin{(\omega_0 t)}$ , the Fourier transform of which would only give us a contribution at  $\omega_0$  but not at higher orders  $N\omega_0$ , where N > 1. Therefore, we can say that the high-harmonic generation due to the intraband current requires an anharmonic band structure. Already the tight-binding approximation for a single neighboring atom gives us a band structure of  $\cos{(ka)}$  (Hofmann, 2015) that contains enough anharmonicity to produce higher order harmonics.

Including higher order cosine terms in the band structure (see Eq. 9 and Fig. 1B for an illustration) introduces even more anharmonicity and therefore leads to even higher frequency contents of significant amplitude in the harmonic spectrum (Ghimire et al., 2011, 2012a; Luu et al., 2015).

Moreover, it is common to introduce the Bloch frequency

$$\omega_B = \frac{eaF_0}{\hbar} \xrightarrow{\text{in atomic units}} \omega_B = aF_0 \tag{17}$$

in Eq. (15), thus obtaining (Luu et al., 2015)

$$I_{HHG,N}(\omega) \propto \left| N\omega_0 \sum_{l=1}^{\infty} lac_l J_N \left( \frac{l\omega_B}{\omega_0} \right) \right|^2.$$
 (18)

The introduction of the Bloch frequency is closely related to the interpretation of the intraband contribution to the HHG yield being due to Bloch oscillations. An introduction to the concept of Bloch oscillations seems therefore appropriate and will follow in the next section.

#### 2.2.3 Understanding Bloch oscillations

Bloch oscillations are an effect that arises when electrons are driven by a constant electric field in a periodic band structure (Bloch, 1929; Zener, 1934). In the previous section, the driving field was not constant but sinusoidal, which leads to a very similar effect that some call "dynamical Bloch oscillations" (Földi et al., 2013; Ghimire et al., 2014; Hohenleutner et al., 2015; Kruchinin et al., 2018; Schubert et al., 2014; Silva et al., 2018; Yoshikawa et al., 2017; Zhang et al., 2019) or "ac Bloch oscillations" (Ghimire and Reis, 2019) to account for the time dependence in the driving field. For an intuitive understanding of Bloch oscillations, however, we will stick to the original setting for Bloch oscillations and use a constant driving field.

Now, let us assume that we have a periodic band partially filled with electrons, which are depicted as green dots in the bottom row of Fig. 2. According to Eq. (4), a constant electric field  $-F_0$  leads to a linear increase of the k-value of these electrons:

$$\frac{\mathrm{d}k(t)}{\mathrm{d}t} = -(-F_0) = F_0 \quad \Rightarrow \quad k(t) = F_0 \cdot t \tag{19}$$

In the bottom row of Fig. 2, this corresponds to the electrons moving to the right in k-space. The group velocity,  $d\mathcal{E}(k)/dk$ , also changes in this process (see the top row of Fig. 2). Assuming a cosine band structure,  $\mathcal{E}(k) = 2 - \cos(ka)$ , we can see that the group velocity,

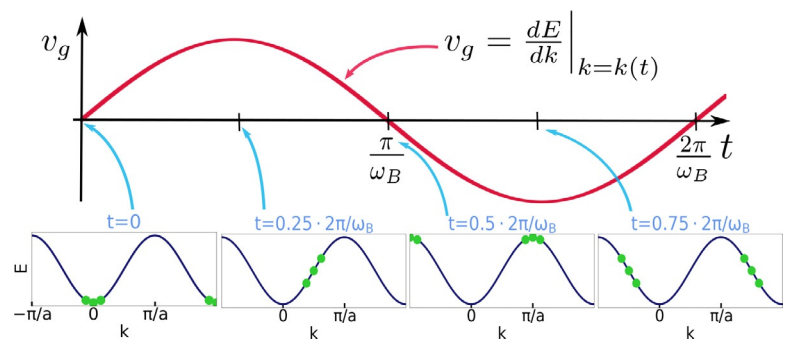


**Fig. 2** Illustration of Bloch oscillations. A constant electric field will monotonically increase the electrons' k values, but the corresponding group velocity  $v_g = dE/dk$  will change periodically in this process and will also have negative values. The change in the sign of  $v_g$  corresponds to a sign reversal of the wave packet's motion in real space. Thus, the electron is reflected back and forth in real space and oscillates within a confined space. The depiction follows the idea presented in the online note (Hofmann, 2014) accompanying Hofmann (2015).

$$\nu_g(t) = \frac{\mathrm{d}\mathcal{E}(k)}{\mathrm{d}k} = a\sin(ka) = a\sin(F_0 \cdot t \cdot a) = a\sin(\omega_B t),\tag{20}$$

does not simply increase further and further as time increases, in contrast to acceleration of electrons by a constant force in free space. Rather, the group velocity oscillates with frequency  $\omega_B$ . This so-called Bloch oscillation can be seen in the top panel of Fig. 2, with  $\omega_B = aF_0$  being the Bloch frequency we already introduced in Eq. (17).

Fig. 2 also gives us an intuitive understanding of the origin of the Bloch oscillation. It shows how the group velocity first increases as the time t, and thus  $k = F_0 t$ , increases. When the electrons reach the inflection point in the periodic band structure  $\mathcal{E}(k)$  (in Fig. 2 at  $t = 0.25 \cdot 2\pi/\omega_B$ ), the group velocity has reached its maximum. And if we go further in time, the electrons reach the edge of the Brillouin zone ( $k = \pi/a$ ) and even change the sign of their group velocity. Thus, we obtain an AC current by applying a DC field and the frequency of this AC current increases with the field strength of the driving field and the lattice constant.

Also note that the sign reversal of the group velocity in the Bloch oscillation (observed at  $t = \pi/\omega_B$  in Fig. 2) corresponds to a reflection in real space (Földi et al., 2013), which results in confinement of the electron wave packet (Ghimire et al., 2012a). The resulting localization of the electrons around the atomic sites in a crystal is also referred to as Wannier-Stark localization (Ghimire et al., 2014; Higuchi et al., 2014; Kogar, 2016; Tancogne-Dejean et al., 2017a). This Wannier-Stark description is equivalent to the

semiclassical Bloch picture we are using here and the quantum mechanical nature of the Wannier-Stark representation shows that the semiclassical Bloch oscillations can be viewed as a rigorous quantum mechanical result (Rossi, 1998).

So far, we assumed a constant driving field, but the result is similar for an oscillating driving field (Földi et al., 2013). The group velocity will still change its sign as the wave packet reaches the maximum of the dispersion relation, the Brillouin zone edge, and will thus have an oscillatory character, albeit with a slightly different equation (compare Eqs. 14 and 20).

In the oscillating driving field, we also have to consider that if the driving field is not sufficiently strong and changes sign before the electron reaches the Brillouin zone edge, no Bloch oscillations can take place simply because the electrons never reach the Brillouin zone boundary. For  $F(t) = F_0 \cos(\omega_0 t)$  and an electron starting at k = 0, we have  $k(t) = -F_0/\omega_0 \sin(\omega_0 t)$  and the critical field strength to observe Bloch oscillations is therefore attained when the amplitude in k, which is  $F_0/\omega$ , equals the Brillouin zone edge,  $\pi/a$  (Ikemachi et al., 2017)

$$\frac{F_0}{\omega_0} \ge \frac{\pi}{a} \Rightarrow F_0 a \ge \pi \omega_0 \Rightarrow \omega_B \ge \pi \omega_0. \tag{21}$$

If this condition is fulfilled, then a full Bloch oscillation can occur within less than a single half cycle of the field because then we also fulfill  $\omega_B \ge 2\omega_0$  (Ghimire et al., 2012a, 2014).

#### 2.3 Details on the interband mechanism

As already mentioned in Section 2.1, the interband mechanism can be described by the following three steps: The laser promotes an electron from the valence to the conduction band (step 1), the electron in the conduction band and the hole in the valence band are accelerated by the laser field (step 2), and then the electron-hole pair can recombine giving off light at a frequency corresponding to the energy difference between the conduction and valence band at the k-value where the recombination occurred (step 3) (Vampa et al., 2014).

The interband mechanism can also be understood in terms of its polarization current. The build-up of a polarization results from the electron in the conduction band and the hole in the valence band being driven in opposite directions in real space by the laser field. This spatial separation of a negative and positive charge results in a dipole and thus a polarization

(Vampa et al., 2015d). As the electrons and holes move in space, this polarization is time-dependent and can radiate light.

The polarization current, also called interband current ( $j_{inter}$ ), is obtained as the time derivative of the polarization P(t)

$$j_{inter}(t) = \frac{\partial}{\partial t} P(t).$$
 (22)

The corresponding radiation spectrum is calculated as the modulus square of the Fourier transform of the time derivative of the current, which corresponds to taking the Fourier transform of the dipole acceleration

$$Yield_{inter}(\omega) = \left| FT \left\{ \frac{\partial}{\partial t} j_{inter}(t) \right\} \right|^2 = \left| FT \left\{ \frac{\partial^2}{\partial^2 t} P(t) \right\} \right|^2 \propto \left| \omega^2 \tilde{P}(\omega) \right|^2, \quad (23)$$

where we used that the Fourier transform of the time derivative is proportional to multiplication with  $i\omega$ . Together with the contribution from the intraband current, the total harmonic yield can thus be obtained as

$$Yield(\omega) = \left| FT \left\{ \frac{\partial}{\partial t} j_{intra}(t) + \frac{\partial}{\partial t} j_{inter}(t) \right\} \right|^{2}$$

$$= \left| FT \left\{ \frac{\partial}{\partial t} j_{intra}(t) + \frac{\partial^{2}}{\partial^{2} t} P(t) \right\} \right|^{2} \propto \left| \omega^{2} \tilde{P}(\omega) + i\omega \tilde{j}_{intra}(\omega) \right|^{2}.$$
(24)

It is interesting to note that there does not seem to be consensus on using the Fourier transform of the time derivative of the current to calculate the spectrum (Cheng et al., 2020; Chizhova et al., 2017; Floss et al., 2018; Golde et al., 2008; Lanin et al., 2017; Tancogne-Dejean et al., 2017b), as we also presented it here, but rather one can frequently find the spectrum calculated as the Fourier transform of the current (Hirori et al., 2019; Kilen et al., 2020; Li et al., 2019b; Liu et al., 2017c; Vampa et al., 2015c,d; You et al., 2017c; Yu et al., 2019b and supplementary information of Garg et al., 2016; Kim et al., 2019; Schubert et al., 2014). Not taking the time derivative of the current leads, in Fourier space, to a factor  $\omega$  less than in Eq. (24) and thus to

$$Yield(\omega) \propto \left| i\omega \tilde{P}(\omega) + \tilde{j}_{intra}(\omega) \right|^2.$$
 (25)

Since the factor  $\omega$  is not just a parameter but the variable on which the spectrum depends, the two different definitions result in different harmonic

spectra, which however look very similar when plotted on a logarithmic scale, as is typically done.

Let us go back to the interband dynamics. For the recombination to happen, it is commonly assumed that the electron and hole have to meet in real space (Vampa and Brabec, 2017; Vampa et al., 2015d). This condition will also follow from the semiclassical saddle-point analysis further down. It seems worth noting, though, that it has also been suggested (Ikemachi et al., 2017; Yu et al., 2020) that recollision can happen at any time due to the spatial delocalization of electrons and holes in solids (Yu et al., 2020). A more quantitative picture that falls in between the mentioned extremes of "recombination can only happen at an exact encounter of electron and hole in real space" and "recombination does not depend on the real space positions" was recently given by the idea of imperfect recollisions (Yue and Gaarde, 2020a). There, the real space coordinates of electrons and holes are accounted for but recombination is possible also upon an imperfect overlap of the electron's and hole's wave packet, i.e., their centers do not overlap exactly (Yue and Gaarde, 2020a). The spatial separation of the electron and hole upon recombination constitutes the formation of a dipole, which has a polarization energy. This affects the energy released as photons in the recombination process.

Another relevant point regarding the recombination dynamics is that, in contrast to HHG in the gas phase, the electron does not have to recombine at the lattice site from which it was ionized (Ernotte et al., 2019; Osika et al., 2017). Tracking of the actual dynamics in real space is often done by using a Wannier basis that is localized in real space as opposed to using a representation in delocalized Bloch wave functions (Ernotte et al., 2019; Osika et al., 2017).

As the electron and hole move in the same direction and speed in k-space when driven by the electric field of the laser pulse (Vampa and Brabec, 2017), both are always at the same position in k-space and the evaluation of the energy release upon recombination is straight-forward and defined as the difference between the energy of the conduction and valence band at the position in k-space at which recombination takes place (see Fig. 1C and D). Therefore, when considering only one valence and one conduction band, the minimum and maximum energy of the emitted light is restricted by the minimum and maximum value of the band gap energy. Note that in the intraband mechanism there is no lower limit for the energy of the emitted light, which is also why the so-called below-band gap harmonics, which have an energy lower than the minimum band gap, are

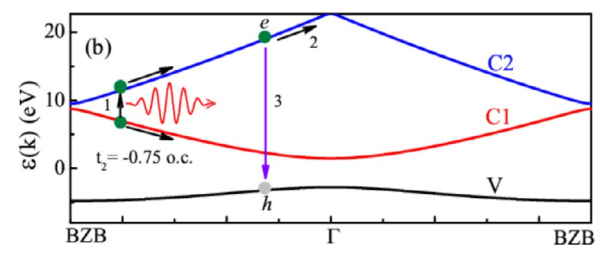


**Fig. 3** Illustration of the electron climbing up to higher conduction bands, thus allowing for higher energies of emitted light upon electron-hole-recombination. V stands for "valence band" and C1 and C2 describe the first and second conduction band, respectively. *Reprinted from Du, T.-Y., Bian, X.-B., 2017. Quasi-classical analysis of the dynamics of the high-order harmonic generation from solids. Opt. Express 25 (1), 151–158.* 

usually assigned to intraband emission (Tancogne-Dejean et al., 2017b). Regarding the maximum possible HHG energies in the interband mechanism one also has to keep in mind that transitions to higher lying conduction bands are possible (Du and Bian, 2017; Ikemachi et al., 2017; Ndabashimiye et al., 2016; Wu et al., 2015; You et al., 2017b; Yu et al., 2020), e.g., by successive promotion into the next higher conduction band, which then allows for a larger energy difference to the valence band and hence higher HHG energies. Fig. 3 shows an illustration of this concept.

#### 2.4 Theoretical methods

Regarding theoretical models for calculating the HHG spectrum, we have so far only described the simple model of the classical electron (or hole) motion in the conduction (valence) band whose anharmonic nature gives rise to an anharmonic current, the intraband current, which radiates high harmonic light. More sophisticated and comprehensive models include effects such as the transition from the valence to the conduction band and back, which then also allows to describe interband harmonic generation and provides a more elaborate framework for the description of intraband harmonic generation.

Most numerical methods are based on solving the time-dependent Schrödinger equation (TDSE), the semiconductor Bloch equations (SBE) or applying time-dependent density functional theory (TDDFT). The variety of numerical methods to describe HHG in solids is increasing quickly and for an in-depth review on just these numerical aspects, we refer the reader to Yu et al. (2019b). Here, we will only briefly summarize the main aspects of the widely applied method of solving the semiconductor Bloch equations.

The semiconductor Bloch equations are a set of coupled integrodifferential equations that describe the optical response of semiconductors to light (Haug and Koch, 2015). They are derived in a fully quantum mechanical framework and describe the interband polarization between conduction and valence band as well as the intraband electric current, from which we can obtain the resulting high harmonic radiation as described in Eq. (24).

Applying a frame transformation (Vampa et al., 2014), we obtain a formulation of the SBE that is easier to integrate numerically and to use in analytical approximations than the standard SBE. The resulting two-band density matrix formulation is then given by Vampa et al. (2014)

$$\dot{\pi}(\mathbf{K},t) = -\frac{\pi(\mathbf{K},t)}{T_2} - i\Omega(\mathbf{K},t)w(\mathbf{K},t)e^{-iS(\mathbf{K},t)}$$
(26)

$$\dot{n}_m(\mathbf{K}, t) = i s_m \mathbf{\Omega}^*(\mathbf{K}, t) \pi(\mathbf{K}, t) e^{i S(\mathbf{K}, t)} + c.c.$$
 (27)

where  $\pi$  represents coherence between the valance and conduction bands (see Eq. 28 for relation to polarization), and  $n_m$  is the valence (m = v) and conduction (m = c) band population, with population difference given by  $w = n_v - n_c$ . It is assumed that initially all electrons are in the valence band, which is described by  $s_m = -1$ , 1 for m = v, c, respectively.  $\mathbf{K} = \mathbf{k} - \mathbf{A}(t)$  and describes that the crystal momentum  $\mathbf{k}$  has been transformed into a frame moving with the vector potential  $\mathbf{A}(t) = -\int \mathbf{F}(t')dt'$  of the laser field  $\mathbf{F}(t)$ , which also shifts the first Brillouin zone:  $\overline{BZ} = BZ - \mathbf{A}(t)$ .  $T_2$  is the dephasing time, which is determined phenomenologically.  $S(\mathbf{K},t) =$  $\int_{-\infty}^{t} \epsilon_g(\mathbf{K} + \mathbf{A}(t')) dt'$  is the classical action, where  $\epsilon_g = E_c - E_{\nu}$  is the crystal momentum-dependent band gap between the conduction band  $E_c$  and the valence band  $E_{\nu}$ .  $\Omega(\mathbf{K}, t) = \mathbf{F}(t)\mathbf{d}(\mathbf{K} + \mathbf{A}(t))$  is the time-dependent Rabi frequency and  $\mathbf{d}(\mathbf{k}) = i \int d^3 \mathbf{x} u_{\nu,\mathbf{k}}^*(\mathbf{x}) \nabla_{\mathbf{k}} u_{\epsilon,\mathbf{k}}(\mathbf{x})$  the transition dipole, with  $u_{m,\mathbf{k}}$ the periodic part of the Bloch function. The coherence  $\pi$  between the valence and conduction bands is related to the polarization between those bands as follows:

$$\mathbf{p}(\mathbf{K},t) = \mathbf{d}(\mathbf{K} + \mathbf{A}(t))\pi(\mathbf{K},t)e^{iS(\mathbf{K},t)} + c.c.$$
 (28)

Applying the Keldysh approximation which assumes  $w(t) \approx 1$ , i.e., neglects depletion of the valence band, leads to a decoupling of Eqs. (27) and (26). The resulting time-dependent polarization, p(t), and population,  $n_m$ , of the

bands can be used to calculate the interband and intraband current according to Eqs. (22) and (11)

$$\mathbf{j}_{intra}(t) = \sum_{m=c,v} \int_{\overline{BZ}} \mathbf{v}_m(\mathbf{K} + \mathbf{A}(t)) n_m(\mathbf{K}, t) d^3 \mathbf{K},$$

$$\mathbf{j}_{inter}(t) = \frac{d}{dt} \int_{\overline{BZ}} \mathbf{p}(\mathbf{K}, t) d^3 \mathbf{K}.$$
(29)

Substituting in the results for p(t) and  $n_m$  from the SBE, transforming back into the original Brillouin zone via  $\mathbf{k} = \mathbf{K} + \mathbf{A}(t)$ , and performing a Fourier transform yields:

$$\mathbf{j}_{intra}(\omega) = \sum_{m=\epsilon, \nu} s_m \int_{BZ} d^3 \mathbf{k} \, \mathbf{v}_m(\mathbf{k}) \int_{-\infty}^{\infty} dt e^{i\omega t} \int_{-\infty}^{t} dt' \mathbf{F}(t') \mathbf{d}(\kappa_{t'})$$
(30)

$$\times \int_{-\infty}^{t'} dt'' \mathbf{F}(t'') \mathbf{d}^*(\kappa_{t'}) e^{-iS(\mathbf{k},t'',t') - (t'-t'')/T_2} + c.c., \tag{31}$$

$$\mathbf{j}_{inter}(\boldsymbol{\omega}) = \boldsymbol{\omega} \int_{BZ} d^3 \mathbf{k} \, \mathbf{d}(\mathbf{k}) \int_{-\infty}^{\infty} dt e^{i\boldsymbol{\omega}t} \int_{-\infty}^{t} dt' \mathbf{F}(t') \mathbf{d}^*(\kappa_{t'}) e^{-iS(\mathbf{k},t',t) - (t-t')/T_2} + c.c.,$$
(32)

with  $\kappa_{t'} = \mathbf{k} + \mathbf{A}(t') - \mathbf{A}(t)$  and  $S(\mathbf{k}, t', t) = \int_{t'}^{t} \epsilon_g(\kappa_{\tau}) d\tau$ . In order to gain a better understanding for the lengthy integrals of Eqs. (32) and (31), it is helpful to interpret t' as the time of electron's transition from the valence to the conduction band and t as the time of observation.

Realizing that the term  $\int_{-\infty}^{\infty} dt e^{i\omega t}$  is just the Fourier transform, we can compare Eq. (32) with the dipole x(t) of Lewenstein's strong-field approximation model for HHG in the gas phase (see eq. 8 in Lewenstein et al., 1994)

$$x(t) = i \int_0^t dt' \int d^3 \mathbf{p} F(t') d_x(\mathbf{p} - \mathbf{A}(t')) d_x^*(\mathbf{p} - \mathbf{A}(t)) e^{-iS(\mathbf{p}, t, t')} + c.c.$$
(33)

finding strong similarities between these two expressions (Amini et al., 2019). This provides a more formal illustration of the close analogy between the three-step model for HHG in the gas phase and the three-step model for HHG in solids.

For HHG in solids we can, therefore, just as for atomic HHG, apply the saddle point approximation in order to identify the most relevant contributions to the integrals of Eqs. (32) and (31). To determine the saddle points we

have to derive the arguments in the exponential, including the semiclassical action

$$S(\mathbf{k}, t', t) = \int_{t'}^{t} E_{\epsilon}(k + A(\tau) - A(t)) - E_{\nu}(k + A(\tau) - A(t)) d\tau, \qquad (34)$$

with respect to  $\mathbf{k}^3$ , t', and t (Vampa et al., 2014):

$$\nabla_{\mathbf{k}} S(\mathbf{k}, t', t)$$

$$= \int_{t'}^{t} \left[ \nabla_{\mathbf{k}} E_{\epsilon}(\mathbf{k} + A(\tau) - A(t)) - \nabla_{\mathbf{k}} E_{\nu}(\mathbf{k} + A(\tau) - A(t)) \right] d\tau$$

$$= \int_{t'}^{t} \left[ \nu_{\epsilon}(\tau) - \nu_{\nu}(\tau) \right] d\tau = \Delta x_{\epsilon} - \Delta x_{\nu} = 0$$

$$\frac{d}{dt'} \left( S(\mathbf{k}, t', t) + \frac{1}{-i} \frac{-(t - t')}{T_{2}} \right)$$

$$= E_{\nu}(\mathbf{k} + A(t') - A(t)) - E_{\epsilon}(\mathbf{k} + A(t') - A(t)) + i/T_{2}$$

$$= -\epsilon_{g}(\mathbf{k} + A(t') - A(t)) + i/T_{2} = 0$$

$$\frac{d}{dt} \left( S(\mathbf{k}, t', t) + \frac{1}{-i} \frac{-(t - t')}{T_{2}} + \frac{i\omega t}{-i} \right) = E_{\epsilon}(\mathbf{k}) - E_{\nu}(\mathbf{k}) - i/T_{2} - \omega = 0$$
(35)

In principle, these three equations are coupled and have to be fulfilled at the same time. Also, even if we neglect the dephasing terms by setting  $T_2 = \infty$ , we can see that, e.g., the second equation does not have a solution in real space since the band gap  $\epsilon_g$  is not 0 for any real value k. Thus, the resulting saddle points  $k_s$ ,  $t_s'$  and  $t_s$  are in general complex and each of the above equations has a real and imaginary part of the equation, resulting in a total of 6 coupled equations (Vampa et al., 2015d). The complex nature is linked to classically forbidden tunneling from the conduction to the valence band (Vampa et al., 2014, 2015d).

To first order, however, we can neglect the equations for the imaginary parts, which gives an approximation for the classical electron and hole trajectories after tunnel ionization (Vampa et al., 2015d). At least this helps us understand the first of the above saddle point equations. Its interpretation is that recombination only takes place if the electron ( $\Delta x_c$ ) and hole ( $\Delta x_v$ ) meet in real space. Note that, in contrast to the motion in k-space, in real space the electron and hole are driven into opposite directions under influence of the laser field, meaning they are first driven apart and, after the laser field changes its sign, are driven toward each other. Keep in mind that this condition is only derived in a saddle point approximation and is true for the most likely

trajectory, and only when neglecting the imaginary part of the saddle point equations. As discussed at the beginning of this section, imperfect collisions in real space (Yue and Gaarde, 2020a), for example, can also lead to recombination.

In the interpretation of the second and third equations, we will neglect dephasing effects by setting  $T_2 = \infty$ . The second equation is searching for the saddle point of the ionization time t'. As the band gap,  $\epsilon_g$ , is nonzero, we have to resort to using a complex ionization time t'. Its complex nature is indicative of the classically forbidden tunneling process (Vampa et al., 2014). To obtain a classical picture despite the finite band gap, let us assume that the electron tunnels where the band gap has its minimum, which in direct band-gap materials is at the  $\Gamma$ -point, where the crystal momentum is zero (Vampa et al., 2015d). This gives us

$$\mathbf{k} + \mathbf{A}(t') - \mathbf{A}(t) = 0 \Leftrightarrow \mathbf{k} = \mathbf{A}(t) - \mathbf{A}(t'), \tag{36}$$

which equals the equation for the classical electron motion in a solid that we have already seen in Eq. (8). Looking at Eq. (36) as a function of time, we can say that the electron-hole pair is created at zero momentum at time t' (at the  $\Gamma$ -point, in a direct band-gap material) (Vampa et al., 2015d).

The interpretation of the last saddle point equation is again more straight-forward and tells us that the energy  $\omega$  of the emitted photon equals the band gap at the crystal momentum of recombination. Thus, this last saddle point equation can be viewed as an equation ensuring conservation of energy.

Note that all three saddle-point equations modeling HHG in solids have an exact analogue to a corresponding process in isolated atoms, as originally introduced in Lewenstein et al. (1994).

# 2.5 The role of the dephasing time

After having neglected the dephasing time  $T_2$  in the last section, we will discuss the role of this parameter now.

Accounting for dephasing by introducing a parameter  $T_2$  into the SBE (Vampa et al., 2014) is a way to phenomenologically describe that excited electrons in a solid will suffer disruptions, e.g., due to elastic and inelastic scattering with, for example, phonons, crystal defects, impurities, or other electrons (Floss et al., 2019). Since it is extremely difficult to calculate the dephasing time based on the disruption processes, it is common to simply choose a dephasing time that leads to the best agreement between theoretical

and experimental HHG spectra (Du et al., 2018; McDonald et al., 2015b; Nishidome et al., 2020; Vampa et al., 2014, 2015a; You et al., 2018). The effect of the dephasing time on the HHG spectrum may be used, the other way around, to learn about microscopic scattering parameters (Du, 2019) or the degree of disorder in the crystal (Orlando et al., 2020) from a measured spectrum.

As can be seen from the two examples in Fig. 4, a shorter dephasing time leads to cleaner peak formation in the plateau region (Vampa et al., 2014, 2015d). Note that this is true for both inter- and intraband contributions, both shown in the left panels of Fig. 4 (see Section 2.7 for comparison of these two mechanisms). The reason for the cleaner peaks is that a shorter dephasing time allows fewer "trajectory" paths to contribute to the same harmonic (Ivanov and Smirnova, 2013), e.g., because multiple recollisions (Vampa et al., 2015d) or long trajectories are suppressed (Kim et al., 2019). More generally, choosing a shorter dephasing time has been found to resolve the discrepancy between the experimental spectra showing clean peaks in the plateau region and the theoretical spectra, which, in the absence of dephasing, shows strong fluctuations with hardly any pattern. However, the origin of the mystery around the clean peak formation that is seen in the experiment but is difficult to reproduce in calculations (Floss et al., 2018, 2019) is not entirely solved yet. Floss et al. (2018), for example, recently claimed that it is the spatiotemporal distribution of the emission events on the mesoscopic scale that leads to the formation of a clean high-order harmonic spectrum with pronounced peaks at odd harmonics. Dephasing times on the order of 1 fs are neither necessary nor justified for forming a well-defined harmonic spectrum, are the result of this study, and their simulation suggests that the dephasing time is at least one order of magnitude larger, on the order of 10 fs (Floss et al., 2018). Concerns regarding ultrashort dephasing times can also be found in Luu et al. (2015) (see supplementary information therein), where a dephasing time in the regime of 27 fs is suggested, which equals the phonon oscillation period of the system used in this experiment.

So far, determining the dephasing time based on microscopic physical processes in a quantitative way has remained elusive as such a study is complicated due to the many parameters dephasing can depend on, such as electron-electron correlations, dopants, or the temperature (Du et al., 2018). Nonetheless, a number of recent studies has led to better understanding of dephasing time (Floss et al., 2018, 2019; Kilen et al., 2020; Orlando et al., 2020).

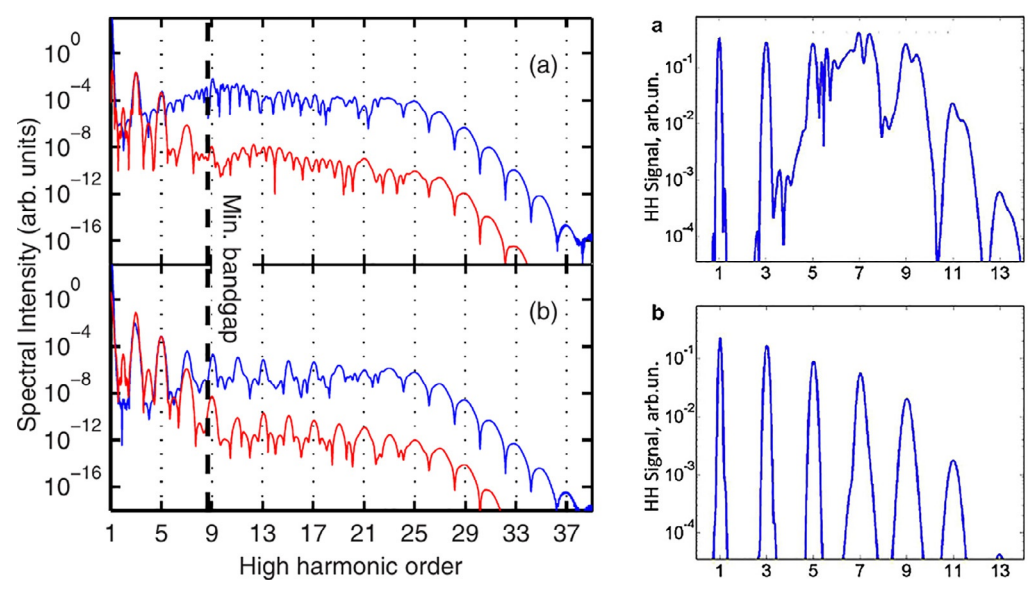


Fig. 4 Simulation results highlighting the role of the dephasing time. We can see that shorter dephasing times lead to cleaner harmonics in the plateau region. Left panels: Dephasing times of (A)  $T_2 = \infty$  and (B)  $T_2 = T_0/4$ , with  $T_0$  the period of the driving laser. The blue lines represent the interband contribution, the red lines the intraband contribution. Both contributions exhibit clear harmonic peaks in the plateau regions for (B)  $T_2 = T_0/4$  but not for  $T_2 = \infty$ . Right panels: HHG spectra for a system different from the one in the left panels. A dephasing time larger than 7 fs (A) and a dephasing time below 2 fs (B), where the latter is shorter than one optical cycle of the driving laser in this case, are chosen. Again we observe that the shorter dephasing time leads to a clearer peak formation. Left Panels: Reprinted figure with permission from Vampa, G., McDonald, C. R., Orlando, G., Corkum, P. B., Brabec, T., 2015d. Semiclassical analysis of high harmonic generation in bulk crystals. Phys. Rev. B 91 (6), 064302. Copyright (2015) by the American Physical Society Right Panels: Reprinted from Ivanov, M., Smirnova, O., 2013. Opportunities for sub-laser-cycle spectroscopy in condensed phase. Chem. Phys. 414, 3–9. Copyright (2013), with permission from Elsevier.

#### 2.6 The cutoff

In HHG in the gas phase, the frequency at which the cutoff is found grows linearly with the intensity of the driving laser (Corkum, 1993; Krause et al., 1992; Schafer et al., 1993). In solids, by contrast, the spectral cutoff position is found to depend linearly on the field strength of the driving laser (Ghimire and Reis, 2019; Ghimire et al., 2011; Higuchi et al., 2014; Vampa et al., 2015d; Wu et al., 2015).

In the gas phase, the HHG cutoff scaling linearly with the laser intensity I can be explained by the fact that the maximum acceleration of the electron in the (Coulomb-free) continuum is approximately  $3.17U_p$ , with  $U_p = I/(4\omega_0^2) \propto I$  the ponderomotive energy. As a consequence, the total energy release upon recombination of the electron with the ion is  $I_p + 3.17U_p$  and thus scales linearly with  $U_p \propto I$  (Corkum, 1993; Krause et al., 1992; Schafer et al., 1993).

In the condensed phase, the linear scaling of the HHG cutoff with the maximum field strength  $F_0$  of the driving laser can be explained in both the intraband and interband framework. In the intraband picture, if the electron (or hole) is moving in a single cosine-shaped conduction (or valence) band (i.e.,  $l_{max} = 1$  in Eq. 10), then the frequency cutoff is found at the order

$$N_{cutoff} = \frac{\omega_B}{\omega_0} = \frac{F_0 a}{\omega_0}.$$
 (37)

If higher cosine terms up to arbitrary order  $l_{max}$  are relevant for the description of the band structure, then the cutoff is found at the harmonic order (Ghimire et al., 2011)

$$N_{cutoff} = \frac{l_{max}\omega_B}{\omega_0} = \frac{l_{max}F_0a}{\omega_0}$$
 (38)

which, when comparing to the last line in Eq. (10), is found to correspond to  $J_N(l_{max}\omega_B/\omega_0)$  being almost constant for harmonic orders  $N=(2n-1) \le l_{max}\omega_B/\omega_0$  and suddenly dropping for harmonic orders  $N>l_{max}\omega_B/\omega_0$ .

In the interband picture, the range of harmonic energies is limited by the band gap energy between the valence and conduction band. The cutoff

<sup>&</sup>lt;sup>a</sup> One may explain this by the upper limit for the Bessel function  $J_{\nu}(x)$  being found at  $\min\{b\nu^{-1/3},c|x|^{-1/3}\}$  with  $b\approx 0.675$  and  $c\approx 0.786$  (Krasikov, 2006; Landau, 2000). Thus, for  $\nu < x$  the minimum is determined by  $c|x|^{-1/3}$ , which does not change with x if x is constant, corresponding to a fixed  $l_{max}$  in  $J_N(l_{max}\omega_B/\omega_0)$ , and consequently to  $J_N(l_{max}\omega_B/\omega_0)$  being almost constant for  $N \le l_{max}\omega_B/\omega_0$ . In contrast, for  $\nu > x$ , the minimum is determined by  $b\nu^{-1/3}$  and is quickly dropping with increasing  $\nu$  that corresponds to an increasing harmonic order N that is greater than  $l_{max}\omega_B/\omega_0$ .

frequency can fall within this allowed range and has been explained via a model in which a linear expansion in k of the conduction and valence band structure is done, and applying Eq. (8) gives a linear dependence of the crystal momentum k at the instance of recombination on  $F_0/\omega_0$  (Vampa et al., 2015d). Consequently also the energy difference between the valence and conduction band upon recombination scales linearly with  $F_0/\omega_0$  under these assumptions.

The observation of multiple plateaus and thus multiple cutoffs in the HHG spectrum can also be explained in the interband framework with electrons climbing up to higher conduction bands (see Fig. 3), thus increasing the energy gap to the valence band (Du et al., 2016; Guan et al., 2016; Jia et al., 2017; Mrudul et al., 2019; Ndabashimiye et al., 2016; Wu et al., 2015, 2016).

The dependence of the cutoff on the wavelength is more contentious than its dependence on the field strength (Liu et al., 2017c). From our discussion of the cutoff in the intra- and interband picture above, one may conclude that the cutoff scales linearly with  $\lambda \propto 1/\omega_0$  in both frameworks. While some publications find such a linear dependence of the cutoff on the wavelength dependence (Chizhova et al., 2017; Guan et al., 2016; Liu et al., 2017c; Vampa et al., 2015d; Wu et al., 2015), others claim there is no wavelength dependence (Ghimire et al., 2012a, 2014; Tancogne-Dejean et al., 2017b). Also, in Liu et al. (2017c) it was observed in numerical computations that the wavelength dependence of the cutoff differs between harmonic light produced in the interband and intraband mechanism.

#### 2.7 Intraband versus interband

Now that we have described the mechanism of HHG due to the intraband and interband mechanism, the obvious question is how much these two mechanisms contribute to the high harmonic light emission. This question has been hotly debated over many years now (Garg et al., 2016; Ghimire et al., 2011, 2012a; Golde et al., 2008; Hawkins et al., 2015; Higuchi et al., 2014; Hohenleutner et al., 2015; Langer et al., 2016; Luu et al., 2015; Schubert et al., 2014; Tamaya et al., 2016; Tancogne-Dejean et al., 2017b; Vampa and Brabec, 2017; Vampa et al., 2014, 2015b, 2020; Wu et al., 2015, 2016; You et al., 2017a,b,c) and even though we will look at characteristics that indicate the dominance of one or the other mechanism in this section, there is still no consensus on this topic.

The reason for the debate despite the difficulties of finding an unequivocal answer is the relevance of this question. Identifying the relative contributions of inter- and intraband HHG is necessary for modeling the experimental results theoretically. And correct theoretical modeling is indispensable when we want to use the emitted high harmonic light to learn about parameters determining the electronic response, such as the band structure (Lanin et al., 2017; Vampa et al., 2015a), or when trying to control the attosecond pulse generation (Ghimire and Reis, 2019) and when thinking about applications in optoelectronics (Garg et al., 2016). Therefore, in the following, we will provide an overview of common arguments in the debate regarding the role of interband and intraband contributions.

The most straight-forward approach to disentangle inter- and intraband contributions is to use a theory that allows to separately calculate the HHG yield from the inter- and intraband mechanism (Vampa et al., 2014; Wu et al., 2015), such as the semiconductor Bloch equations discussed in Section 2.3. The result often obtained this way is that the intraband mechanism dominates the low-frequency regime below the band gap, whereas the interband mechanism is stronger in producing frequencies above the band gap in the plateau region (Jürß and Bauer, 2019; Lanin et al., 2017; Vampa et al., 2014, 2015c; Wu et al., 2015). Examples of this can be found in the left panel of Fig. 4 above or the top panel of Fig. 5 in Wu et al. (2015). We can understand the dominance of the intraband contribution in the below-band-gap regime in the recollision picture of the interband mechanism in which the energy release is restricted by the range of energy differences between the valence and the conduction bands.

Using a theory that separates the inter- and intraband contribution, however, does not necessarily give a clear answer to the relative contributions of the two mechanisms to the measured high harmonic yield. For example, in the semiconductor Bloch equations discussed in Section 2.3, the relative role of inter- and intraband depends on, e.g., the dephasing time (Almalki, 2019), which we do not know how to choose in a physically meaningful way (see Section 2.5). Problems also arise from the fact that the interband and intraband contributions are coupled (Al-Naib et al., 2014; Ghimire and Reis, 2019; Golde et al., 2008; Guan et al., 2019; Tancogne-Dejean et al., 2017a; Wu et al., 2015; Zuo et al., 2019), especially at higher driving field strengths (Ghimire and Reis, 2019; Wu et al., 2015), and a separation may not be valid. Földi (2017), for example, claims that gauge transformations, which by design do not affect the actual physics, mix the inter- and intraband dynamics.

Another popular way to study the role of the interband and intraband mechanism is to investigate whether the high harmonic light exhibits a chirp, i.e., whether its frequency changes with time (Garg et al., 2016; Li et al., 2020; Vampa and Brabec, 2017; Vampa et al., 2015b, 2020; Wu et al., 2015; You et al., 2017b,c). Light produced in the interband mechanism is expected to have a chirp, whereas the light from the intraband mechanism has a negligible chirp (Garg et al., 2016; Li et al., 2020; Vampa and Brabec, 2017; Vampa et al., 2015b, 2020; Wu et al., 2015; You et al., 2017b,c). An example of a time-frequency analysis giving this result is shown in Fig. 5, where the tilt of the "blob" in the case of the interband high harmonic indicates that different frequencies (i.e., harmonic orders) are emitted at different times, meaning we observe a chirp.

How can we understand that the interband mechanism leads to a chirp but the intraband mechanism does not? In the interband mechanism, the recombination time varies on a subcycle scale depending on the energy of the electron-hole pair, similar to the situation in HHG with atoms where the kinetic energy of the electron corresponds to different recombination time (Vampa et al., 2020). Thus, a chirp is observed due to the different

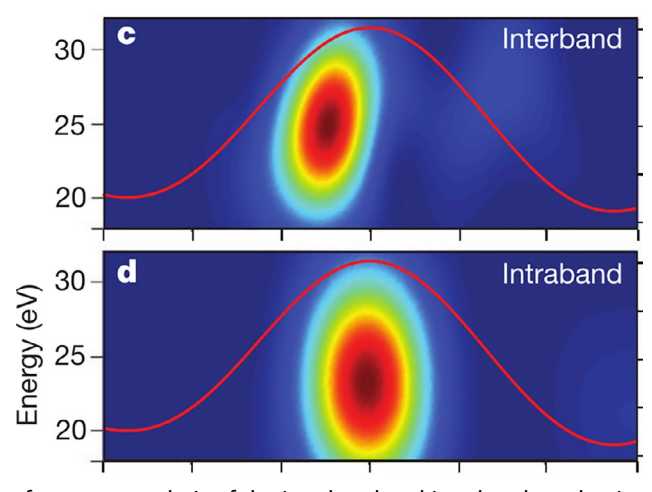


**Fig. 5** Time-frequency analysis of the interband and intraband mechanism. The tilt of the "blob" in the interband mechanism indicates that different harmonics are emitted at different times, corresponding to a chirp. The intraband mechanism, in contrast, does not show a significant chirp. Reprinted by permission from Springer Nature Customer Service Centre GmbH: Springer: Garg, M., Zhan, M., Luu, T. T., Lakhotia, H., Klostermann, T., Guggenmos, A., Goulielmakis, E., 2016. Multi-petahertz electronic metrology. Nature 538 (7625), 359363. Copyright (2016).

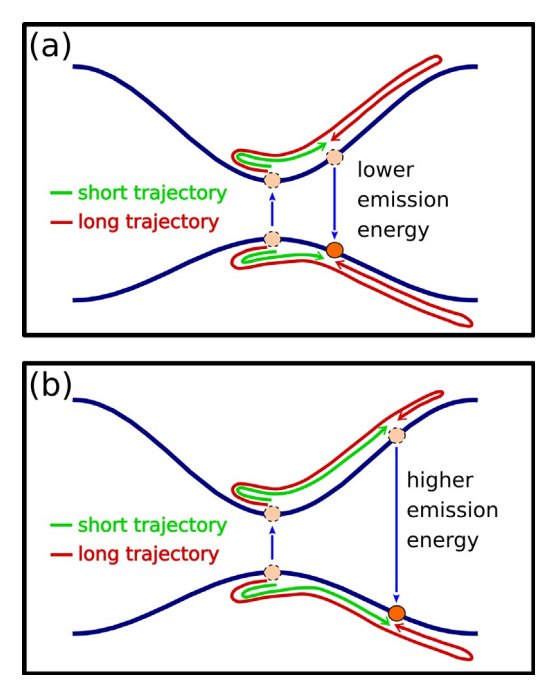


**Fig. 6** Illustration explaining the positive chirp observed in case of dominance of short trajectories and the negative chirp in case of dominance of long trajectories. Panels (A) and (B) represent two situations leading to a lower (A) or higher (B) emission energy. In both cases we look at the short trajectories (*green*) and long trajectories (*red*). Comparing (A) and (B), we see that the short trajectories (*green*) have a longer excursion time in the case of later recombination followed by higher energy emission. This corresponds to a positive chirp. By the same argument, long trajectories (*red*), emit higher harmonics earlier, corresponding to a negative chirp. As usually short trajectories dominate the HHG spectrum, positive chirps are often observed experimentally.

emission times of the different harmonic orders (Li et al., 2020; Vampa and Brabec, 2017; Wu et al., 2015).

In this framework, we can also understand why higher frequency components are emitted later in time in Fig. 5: We look at short and long trajectories in Fig. 6, which arise in reciprocal space because the same crystal momentum k is passed twice per half cycle (Kim et al., 2019). Short trajectories are related to the first time a specific k is passed, long trajectories are related to the second time (Kim et al., 2019) (see Fig. 6). As illustrated in Fig. 6, for short trajectories (green line) a longer excursion time, thus later recombination, corresponds to recombination at a higher bandgap energy and consequently emission of larger frequencies (Lu et al., 2019). This results in a positive chirp of the emitted light, i.e., the frequency increases

with emission time. For long trajectories, in contrast, a longer excursion time leads to recombination at a smaller bandgap energy, and the emission of smaller frequencies, corresponding to a negative chirp (Liu et al., 2017b). The often observed dominance of contributions from short trajectories to the spectrum (Vampa et al., 2020) helps us understand why chirps observed in HHG in solids are often positive (Garg et al., 2016; Lu et al., 2019; Vampa et al., 2015b, 2020; You et al., 2017b), as, for instance, in Fig. 5.

In the intraband mechanism, in contrast, the various harmonics are emitted at the same time (Wu et al., 2015). This can be seen by looking at the intraband current from Eq. (10). Written in the same way as in Wu et al. (2015), we get

$$j_{intra}(t) = \sum_{n} D_n \sin((2n-1)\omega_0 t), \tag{39}$$

with  $D_n$  depending on the band structure and electric field strength. Thus, we can directly see that in the intraband picture all harmonic orders, corresponding to the different n in Eq. (39), are generated at the same time and thus there is no chirp in the emitted light.

So far, the chirp seems to be the perfect parameter to look at for finding out whether intra- or intraband contributions dominate the spectrum. However, things are more complicated than presented above. For example, additional contributions to the chirp can arise from propagation effects, e.g., due to dispersion and self-phase modulation of the laser pulse (Ghimire et al., 2011). Moreover, the existence or absence of a chirp seems to vary strongly depending on the material parameters. For example, in SiO<sub>2</sub> (Garg et al., 2016) and GaSe (Hohenleutner et al., 2015) no chirp was found, whereas in ZnO (Vampa et al., 2015b) and MgO (Vampa et al., 2020; You et al., 2017b) a chirp was found. Therefore, even though we may now assign dominance of interband or intraband contributions to those systems showing or not showing a chirp, it is not fully clear yet what the reason for these different observations is. In Vampa et al. (2015b), it is claimed that wider bands and higher intensities will result in smaller chirps. And in You et al. (2017b), it was suggested that the reason for varying chirp observations in various materials may have to do with the type of bonding. For example, MgO, a solid with ionic bonding, has a chirp in its HHG emission, while GaSe and SiO<sub>2</sub> have covalent bonds and produce no chirp.

Besides the two most commonly used tools of splitting interband and intraband contributions in theoretical models and analyzing the chirp, occasionally other observables are used to determine whether the interband or intraband mechanism dominates. In Liu et al. (2017a), for instance, the Berry curvature gives rise to even harmonics which are predominantly polarized perpendicular to the pump laser and are compatible with the intraband theory, whereas the weak parallel component of the emitted light indicates interband transitions. Or in Han et al. (2019), for example, a differing dependence of the interband and intraband contribution on the crystal orientation was observed. Comparison with orientation-resolved experimental data allowed to determine whether interband or intraband contributions dominate in the studied system.

Another angle for investigating interband and intraband contributions is taken in Yoshikawa et al. (2019), which uses resonances that play a role in the interband mechanism but are absent in the intraband theory. The enhancement of the HHG yield at energies that are in resonance with the optical transition was therefore interpreted as a strong interband contribution. Furthermore, the observation that the ellipticity of the driving laser affects interband and intraband contributions differently was used to learn about the dominant mechanism underlying HHG in solids (Ndabashimiye et al., 2016; Tancogne-Dejean et al., 2017a).

Despite all of the mentioned efforts to disentangle the interband and intraband contributions to the measured high harmonic light, there is still no consensus on which mechanism dominates or what tests to use to determine the dominant mechanism. One problem in the discussion seems to arise from the possibility that the relative role of the inter- and intraband mechanism depends on laser and material parameters, which complicates matters. Besides the material dependence of the chirp mentioned above, the spectral range of the driving laser is also thought to affect how interand intraband contribute (Guan et al., 2019; Lanin et al., 2017; Vampa et al., 2014; Yu et al., 2019b). Vampa et al. (2014) does an in-depth theoretical analysis of the wavelength dependence and finds that interband contributions dominate at smaller wavelengths but intraband contributions become relevant at longer wavelengths. Similarly, in a pump-probe experiment with the pump injecting photo-carriers (Wang et al., 2017), interband contributions were found to dominate at smaller wavelengths, but at longer wavelengths, with all other parameters kept constant, the intraband mechanism starts to dominate. This effect can be understood by the longer wavelength leading to a longer excursion time (t - t') (compare Eq. 32) and thus the dephasing will suppress the interband contributions more strongly (Vampa et al., 2014; Wang et al., 2017). Also, the longer excursion time enhances quantum spreading of 3D electron and hole wave packets, which

reduces recollision probability (Vampa et al., 2014). The tendency of interband dominating at smaller wavelengths and intraband at longer wavelengths can also be seen by comparing different studies of ZnO (Lanin et al., 2017): In Vampa et al. (2015b), Vampa et al. (2014), Vampa et al. (2015a), and Wang et al. (2017), for (relatively) short wavelengths around  $\lambda = 3.7~\mu m$ , interband is found to dominate. In Hohenleutner et al. (2015) and Schubert et al. (2014), at a THz driving pulse, in contrast, the intraband mechanism explains the results.

To complete this section, we mention two other contributions that were recently found to play a role beside the intra- and interband mechanism. Zhao et al. (2020) suggest that the interband current between various conduction bands, as opposed to the interband current between conduction and valence band, contributes to the high harmonic emission. Moreover, Jürgens et al. (2020) find that the nonlinear response emerging from the subcycle injection dynamics of electrons into the conduction band contributes to the below-band-gap harmonics.

## 2.8 Comparison of HHG in gases and solids

As there already are a number of publications (e.g., Amini et al., 2019; Ghimire and Reis, 2019; Ghimire et al., 2014; Hansen et al., 2018; Huttner et al., 2016; Li et al., 2020; Ndabashimiye et al., 2016; Tancogne-Dejean and Rubio, 2018; Tani et al., 2020; Vampa and Brabec, 2017; Vampa et al., 2015b,c), and among those also review papers (Ghimire and Reis, 2019; Ghimire et al., 2014; Li et al., 2020; Vampa and Brabec, 2017; Vampa et al., 2015c), that compare HHG in gases and solids in detail, we want to summarize only the most relevant points here.

The reason for frequent comparisons between HHG in solids and the corresponding process in atoms and molecules in the gas phase is twofold. The first reason is mostly historic because HHG in the gas phase is often viewed as the precursor of HHG in solids, and the same attosecond community that studied HHG in the gas phase for decades is now investigating HHG in solids. The second reason is that the 3-step model in HHG in gases is similar to the interband model. Therefore, some features that are similar in HHG in atoms and solids are interpreted as being indicative of the interband mechanism dominating (Ndabashimiye et al., 2016; Vampa et al., 2015d). As we have seen, the strong similarity between the recollision model in solids (i.e., the interband model) and in gases is also reflected in the shape of the equation for the interband polarization current in the solid system bearing

strong resemblance with the equation for the dipole current in atoms (compare Eqs. 32 and 33) (Amini et al., 2019).

However, there are also many differences between HHG in the gas and solid phase. For example, the cutoff scales linearly with the driving laser field strength in solids but quadratically in atomic and molecular systems (see Section 2.6). This discrepancy also tells us that although there may be similarities between the mechanisms leading to HHG in gases and solids, these mechanisms differ in crucial aspects. One of these aspects is that in solids the periodic band structure can give rise to Bloch oscillations (see Section 2.2), whereas in the gas phase, the electron's energy grows monotonically with electron momentum (if we neglect the Coulomb potential). An illustration of this can be found in Fig. 7. Moreover, we have seen that the nonparabolic

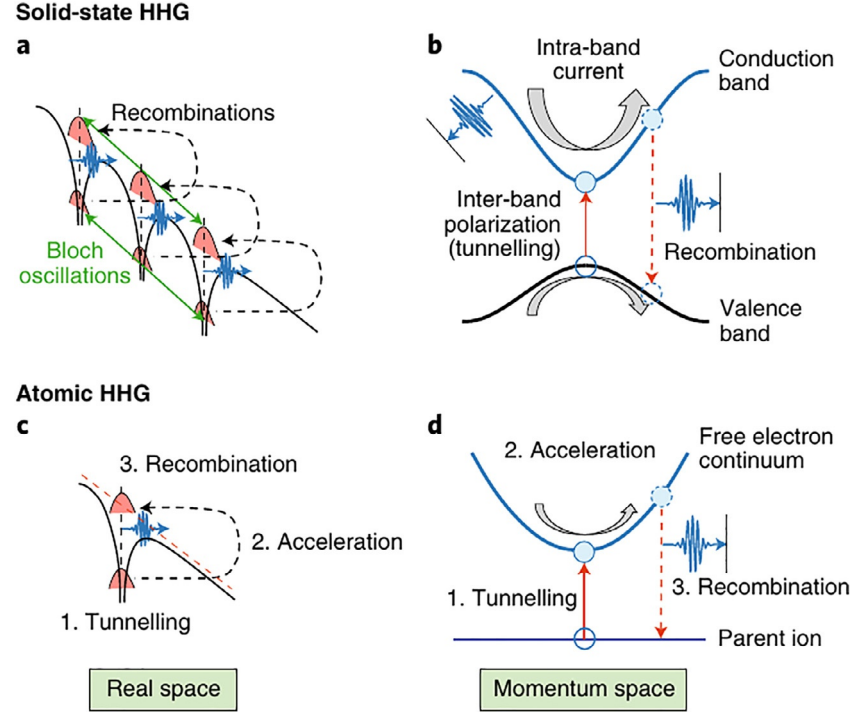


**Fig. 7** Comparison of HHG mechanisms in atoms and solids in real and reciprocal space (= momentum space). The recollision mechanism that explains HHG in the gas phase has its clear analogue in the interband mechanism in solids. The high harmonic light produced in solids due to the anharmonic motion in the periodic band structure (intraband current) is lacking a clear analogue in HHG from gases. *Reprinted by permission from Springer Nature Customer Service Centre GmbH: Springer; Ghimire, S., Reis, D. A., 2019. High-harmonic generation from solids. Nat. Phys. 15 (1), 10–16. Copyright (2019).* 

nature of the band structure is relevant for the higher orders emitted via the intraband mechanism (see Section 2.2) in solids. In contrast, in HHG in the gas phase, the force of the Coulomb potential of the residual ion on the departing electron can be neglected to lowest order (Amini et al., 2019; Ivanov et al., 2005; Lewenstein et al., 1994), which corresponds to a simple parabolic structure of the energy dispersion relation (see Fig. 7D).

Another aspect that is different in the dynamics leading to HHG in gases and solids is that in the gas phase, the remaining positive ion of the atom or molecule is over 1000 times heavier than the electron and therefore hardly moves. Consequently, the kinetic energy of the positive charge in the gas phase HHG can be considered constant, as illustrated in Fig. 7D. In the condensed phase, on the contrary, the hole in the valence band has a comparable effective mass as the electron in the conduction band and its motion has to be taken into account.

Regarding the dynamics, HHG in the gas and condensed phase also differs in that the electron has to return to its parent ion in real space in the gas phase, whereas in the condensed phase there is a nonnegligible possibility that the electron may recombine with a neighboring atom (Osika et al., 2017). This result was obtained in a study (Osika et al., 2017) based on a representation using localized Wannier wave functions in the valence band and delocalized Bloch functions in the conduction band, which allows to analyze at which lattice site recombination takes place. The question of whether the wave packet needs to return to its parent ion for HHG is also directly linked to the effect of using an elliptically polarized driving pulse instead of a linearly polarized one.

In the gas phase, the requirement to return to the parent ion leads to a strong decrease of the HHG yield with increasing ellipticity as the electron tends to drift away and miss the parent ion at higher ellipticity (Budil et al., 1993; Burnett et al., 1995; Kopold et al., 2000). In the condensed phase, there seems no consensus yet on how the ellipticity, and related to this the localization effect just described, affects high harmonic emission: Ghimire et al. (2011) found a significantly weaker dependence of the high harmonic yield on ellipticity in experiments with ZnO than in the gas phase. A stronger decline of HHG yield with ellipticity, that is still weaker than in gases though, was found theoretically in Vampa et al. (2014). On the other hand, Li et al. (2019b) find theoretically that increasing the ellipticity can even enlarge the HHG yield, in contrast to the situation in the gas phase.

Ndabashimiye et al. (2016), on the contrary, found experimentally that the ellipticity dependence of solid argon is comparable to gas-phase argon, supporting the view that the electron recombines with the lattice site at which it transitioned into the conduction band. This is compatible with the observation that solid argon atoms are bonded by weak Van der Waals forces (in contrast to ionic or covalent bonds which commonly hold solids together). Since Van der Waals forces do not involve electron exchange between neighboring atomic sites, the process of HHG is expected to be highly localized, similar to what we see in the atomic gas. It is clear from the above that solids exhibit much more variable behavior that can be strongly dependent on the nature of the chemical bonds that hold them together.

The dynamics of HHG differs in solids and gases also due to the higher density in the condensed phase (Ghimire et al., 2012b, 2014; Luu et al., 2018; Mrudul et al., 2020; Yoshikawa et al., 2017), which can enhance the yield of the emitted light. However, there are also problems in solids that do not exist in the gas phase. For example, the solid sample can suffer damage under too strong radiation. While using a high intensity of the driving laser field would in principle increase the yield of the harmonic light and also the maximum high harmonic order, the use of high intensities is limited by the material's damage threshold (Ghimire and Reis, 2019; Hohenleutner et al., 2015; Liu et al., 2018b; Luu and Wörner, 2016; McDonald et al., 2015a, 2017; You et al., 2017c). Damage occurs if the conduction band population reaches a certain level (McDonald et al., 2017) and therefore the damage threshold can be increased by using large band gap materials, small photon energy (corresponding to longer wavelengths), and a short pulse duration (Ghimire and Reis, 2019; Ghimire et al., 2011; You et al., 2017c). The damage threshold in solids can also be linked to thermal heating as has been suggested by the lower damage threshold in thinner samples (Hohenleutner et al., 2015). The damage threshold problem does not exist in the same way in the gas phase, which is why HHG in solids normally relies on driving pulses with lower intensities and longer wavelengths.

Moreover, in the solid phase, the emitted high harmonic light often suffers from strong self-absorption by the solid as attenuation lengths in the XUV regime are only tens of nanometers long (Ghimire and Reis, 2019). The problem of reabsorption of the emitted light by the medium also exists in the gas phase, though (Constant et al., 1999; Dachraoui et al., 2009; Kazamias et al., 2003; Popmintchev et al., 2009; Rothhardt et al., 2014).

We want to round off this discussion about differences and similarities between HHG in solids and gases by looking at yet another phase: liquids. The generation of high harmonic light from liquids (DiChiara et al., 2009; Heissler et al., 2014; Luu et al., 2018; Wörner et al., 2020) has the advantage

of using a high-density sample, comparable to the density in solids. At the same time, in liquids one can avoid the problem of sample damage by using a liquid jet which continuously renews the irradiated sample (Luu et al., 2018). The cutoff of high harmonics from liquids scales like  $F^{1.2}$ , similar to the  $F^1$  relation observed in solids. The liquid density, which is comparable to the density of solids, may allow one to apply theoretical models to liquids that are also used to explain HHG in solids (Luu et al., 2018). However, the strong disorder in liquids requires modifications in the application of the momentum space description used for solids (Wörner et al., 2020).

# 3. Applying HHG in solids

Besides the obvious application of using HHG in solids as a new light source, the high harmonic light generated in solids carries information about properties of the material, such as the band structure or the nonlinear response of the medium. Thus, HHG in solids can complement methods such as angle-resolved photoemission spectroscopy (ARPES) (Damascelli et al., 2003) that study photoelectrons to learn about the material these electrons were released from. The shortness of the incident laser pulse used in HHG with solids has the advantage of, first, allowing high laser intensities and thus the investigation of the highly nonlinear response of the material to such extreme fields, and second, a high time-resolution.

In the following we review some of the material features that HHG in solids has helped gain access to, as well as give an overview of the large variety of solid state systems where HHG is observed.

# 3.1 Reconstructing the band structure (in reciprocal space)

As we have seen in Sections 2.2 and 2.3, the band structure of the conduction and valence bands directly affects the high harmonic emission in both the interband and intraband mechanisms (Ghimire et al., 2011; Lanin et al., 2017; Luu et al., 2015; Tancogne-Dejean et al., 2017b; Vampa et al., 2015a; Wang et al., 2016). Information about the band structure can therefore be retrieved by analysis of the high harmonic light. In Vampa et al. (2015a), for example, the band structure was reconstructed in an experiment that used two laser pulses, one with frequency  $\omega$  and a much weaker time-delayed second harmonic,  $2\omega$ , in a regime where the interband mechanism dominates. The delay that led to the most intense even harmonics, corresponding to maximum symmetry breaking, was obtained from the experiment and compared to the delay obtained from interband HHG simulations using a

large range of different band structures. The band structure was thus determined by the set of parameters for the band structure that led to the best agreement with the experimental result.

In a complementary approach, Lanin et al. (2017) and Wang et al. (2016) focus on an experimental regime where the intraband mechanism dominates and obtains the band structure by comparing the harmonic yield of the different harmonic orders in the experiment and in theory, again for a scan over a set of parameters describing the band structure in the theoretical calculation. The set of parameters for the band structure that brings the theoretical harmonic yields closest to the experimental yields is then interpreted as the best description of the band structure.

## 3.2 Reconstructing the crystal lattice (in real space)

The band structure describes the crystal structure in the reciprocal space. The high harmonic light emitted from solids can also be used to probe the arrangement of atoms in the crystal lattice (You et al., 2017a, 2018) and the spatial structures within a unit cell in real space (Mrudul et al., 2019). In You et al. (2017a), for example, elliptical light was used to control trajectories in real space, leading to higher (lower) high harmonic yield if the trajectory hits (misses) the neighboring atomic core. This picture of semiclassical electron trajectories in real space also helped understand the microscopic origin of the strongly anisotropic angular distribution observed in the high harmonic yield with linear light in You et al. (2017a), despite the isotropic linear and weakly anisotropic nonlinear optical properties of the cubic crystal in the perturbative regime.

# 3.3 Symmetry effects

So far, we have used a 1D setting for studying HHG in solids, with dimension of interest chosen parallel to the linear polarization of the driving laser field. However, taking into account the 3D geometry and symmetry properties of the crystal or using elliptically or circularly polarized light to break certain symmetries can lead to interesting effects that can be directly seen in, for instance, the symmetry properties of the harmonic spectrum, the appearance of even and odd harmonics or polarization effects.

In the simplest case, the crystal symmetry will be directly reflected in the symmetry of the high harmonic light. If the crystal has *n*-fold rotational symmetry and linearly polarized light impinges on it, we expect *n*-fold symmetry in the harmonic spectrum. An example can be seen in Fig. 8. The effect can

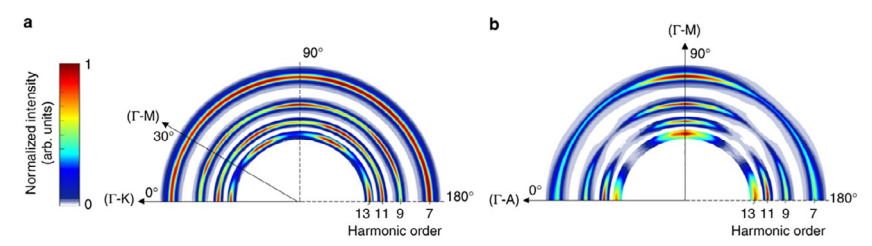


**Fig. 8** High harmonic-generation yield sweeping over the linear polarization direction of the driving laser with respect to the crystal orientation in the C-plane of sapphire. The symmetry properties of the harmonic yield reflect the symmetry properties of the crystal: The harmonic yield exhibits the sixfold symmetry in the C-plane. *Reprinted from Han, S., Ortmann, L., Kim, H., Kim, Y. W., Oka, T., Chacon, A., Doran, B., Ciappina, M., Lewenstein, M., Kim, S.-W., et al., 2019. Extraction of higherorder nonlinear electronic response in solids using high harmonic generation. <i>Nat. Commun. 10 (1), 1–6.* 

easily be understood by one-dimensional cuts of the band structure along the linear polarization of the driving laser field, which will repeat itself with the *n*-fold symmetry of the crystal.

However, effects related to the crystal symmetry can be far more sophisticated (Jia et al., 2017; Jin et al., 2018; Langer et al., 2017; Liu et al., 2017a; Saito et al., 2017; Wu et al., 2017; Zhang and Bai, 2019; Zurrón-Cifuentes et al., 2019). In Langer et al. (2017), for example, using linearly polarized light to drive HHG in GaSe, it was observed that the polarization and the carrier-envelope phase (CEP) of the high harmonic light can be controlled by the crystal symmetry. Further results showing that the crystal symmetry can determine the polarization of the harmonic light were observed in Jiang et al. (2019). Moreover, as even and odd harmonics appear under different symmetry conditions, the possibility arises to separate even and odd harmonics by means of their polarization (Langer et al., 2017; Liu et al., 2017a), which opens new ways for the temporal emission characteristics (Langer et al., 2017).

Using an elliptically or circularly polarized driving pulse instead of a linearly polarized one obviously also changes the overall symmetry of the laser-matter interaction. In Saito et al. (2017), for example, a thin gallium selenide crystal is irradiated by circularly polarized light and the threefold rotational symmetry of the crystal leads to the complete suppression of every third-harmonic order. This is understood by applying the selection rules caused by the rotational symmetry of an HHG medium (Alon et al., 1998; Saito et al., 2017; Tang and Rabin, 1971), which allows only the following harmonic orders

allowed harmonic orders = 
$$nj + \sigma$$
 with  $j \in \mathbb{N}$  (40)

to appear in a crystal of n-fold symmetry under irradiation of a circularly polarized light.  $\sigma$  can be  $\pm$  1 and tells us whether the circular polarization direction of the emitted light is identical ( $\sigma = +1$ ) or opposite ( $\sigma = -1$ ) to the circular polarization direction of the driving field. Applying this selection rule, we can understand the mentioned result of a threefold crystal symmetry not showing harmonic emission at the 3rd, 6th, 9th, ...order.

Similar symmetry concepts apply if the irradiated sample is a 2D monolayer, with additional effects arising if the laser polarization probes the out-of-plane direction (Jin et al., 2018; Liu et al., 2017a; Zhang and Bai, 2019; Zurrón-Cifuentes et al., 2019). Other symmetry effects on HHG that are due to a particular geometry of the sample can be observed in nanostructures. For example, a strong dependence of the HHG light from a nanowire on the orientation of the driving laser field polarization was observed in Li et al. (2019a).

All in all, these examples show that symmetry properties of the crystal can be measured by the properties of the high harmonic emission. And the other way around, tuning the symmetry properties of the crystal and the incident laser can be used to control relevant properties of the harmonic light such as its polarization or the suppression of certain harmonic orders.

# 3.4 Measuring the Berry curvature

Another important material property that can be investigated with HHG in solids is the Berry phase or Berry connection (Chacón et al., 2020; Jia et al., 2020; Liu et al., 2017a; Luu and Wörner, 2018; Yue and Gaarde, 2020a,b). Therefore, let us briefly summarize the concept of the Berry phase (Berry, 1984; Resta, 2000; Xiao et al., 2010; Zwiebach, 2018).

The Berry phase can arise in a system in which the Hamiltonian  $H(\mathbf{R})$  depends on a set of parameters  $\mathbf{R} = \{\mathbf{R}_1(t), \mathbf{R}_2(t), ...\}$  that change adiabatically with time t. In HHG in solids, the changing parameter will be the crystal momentum  $\mathbf{k}$ , but for now let us stick to the more general notation using  $\mathbf{R}$ . Let us assume that we know the eigenstates  $E_n$  for all possible parameter values  $\mathbf{R}$ 

$$H(\mathbf{R})|\psi_n(\mathbf{R})\rangle = E_n(\mathbf{R})|\psi_n(\mathbf{R})\rangle.$$
 (41)

Now, if the value of the parameter  $\mathbf{R}$  changes with time, also our Hamiltonian will be time-dependent. However, the adiabatic theorem allows us to assume that the system will remain in the same eigenstate n (this state may just

evolve in time as R(t) changes) and we can use the instantaneous solutions  $|\psi_n(\mathbf{R}(t))\rangle$  and  $E_n(\mathbf{R}(t))$  for the time-dependent eigenstate and eigenenergy obtained from the time-independent Schrödinger equation (41), where the only degree of freedom is the quantum phase (Xiao et al., 2010)

$$|\Psi_n(t)\rangle = e^{i\theta_n(t)}e^{i\gamma_n(t)}|\psi_n(\mathbf{R}(t))\rangle.$$
 (42)

The phase  $\theta_n(t)$  is called the dynamical phase and it functions as a clock, of sorts, because it changes as the time t changes (Zwiebach, 2018). The phase  $\gamma_n(t)$  is called the geometrical phase, and we will see that, viewed in the right way, it does not depend on the time t but only on the path  $\Gamma$  that we travel in the parameter space  $\mathbf{R}$  as time evolves (Zwiebach, 2018). We can calculate  $\gamma_n(t)$  by plugging  $|\Psi_n(t)\rangle$  into the time-dependent Schrödinger equation, obtaining

$$\gamma_{n}(t) = \int_{0}^{t} i \left\langle \psi_{n}(\mathbf{R}(t')) \right| \frac{d}{dt'} \psi_{n}(\mathbf{R}(t')) \rangle dt' 
= \int_{0}^{t} i \left\langle \psi_{n}(\mathbf{R}(t')) \right| \frac{\partial \psi_{n}}{\partial \mathbf{R}_{1}} \frac{\partial \mathbf{R}_{1}}{\partial t'} + \frac{\partial \psi_{n}}{\partial \mathbf{R}_{2}} \frac{\partial \mathbf{R}_{2}}{\partial t'} + \dots \rangle dt' 
= \int_{0}^{t} i \left\langle \psi_{n}(\mathbf{R}(t')) \right| \nabla_{\mathbf{R}} \psi_{n}(\mathbf{R}) \rangle \frac{d\mathbf{R}}{dt'} dt' 
= \int_{\Gamma} i \left\langle \psi_{n}(\mathbf{R}) \right| \nabla_{\mathbf{R}} \psi_{n}(\mathbf{R}) \rangle d\mathbf{R}.$$
(43)

One can see that the time dependence vanishes in the last line and the phase  $\gamma_n$  only depends on the path  $\Gamma$  in the parameter space from  $\mathbf{R}(t'=0)$  to  $\mathbf{R}(t'=t)$  (Zwiebach, 2018). If this path  $\Gamma$  is not closed, then  $\gamma$  will not be gauge-invariant. For a closed path, i.e.,  $\mathbf{R}(t'=0) = \mathbf{R}(t'=t)$ ,  $\gamma$  becomes gauge-invariant and thus physically meaningful and therefore is given its own name: the Berry phase. The term

$$A_n(\mathbf{R}) = i \langle \psi_n(\mathbf{R}) | \nabla_{\mathbf{R}} \psi_n(\mathbf{R}) \rangle \tag{44}$$

from the bottom row of Eq. (43) is called the Berry connection or the Berry vector potential. The Berry curvature can, in a three-dimensional parameter space, be defined as

$$\mathbf{\Omega}_n(\mathbf{R}) = \nabla_{\mathbf{R}} \times A_n(\mathbf{R}). \tag{45}$$

Applying Stokes' theorem, we can write the Berry phase in terms of this Berry curvature

$$\gamma_n = \oint_{\Gamma} A_n(\mathbf{R}) d\mathbf{R} = \int_{S} d\mathbf{S} \cdot (\nabla_{\mathbf{R}} \times A_n(\mathbf{R})) = \int_{S} d\mathbf{S} \cdot \mathbf{\Omega}_n(\mathbf{R}), \quad (46)$$

where S is the surface enclosed by the path  $\Gamma$ .

In solids, the parameter **R** is the crystal momentum **k** and the equations of motion in a system with a nonvanishing Berry curvature read (Gradhand et al., 2012; Liu et al., 2017a; Luu and Wörner, 2018; Ralph, 2020)

$$\dot{\mathbf{k}}(t) = -e\mathbf{F}(t) \tag{47}$$

$$\dot{\mathbf{r}}(t) = v_g(t) = \frac{\mathrm{d}\mathcal{E}(k)}{\mathrm{d}\mathbf{k}} - \dot{\mathbf{k}} \times \mathbf{\Omega}(\mathbf{k}) = \frac{\mathrm{d}\mathcal{E}(k)}{\mathrm{d}\mathbf{k}} + e\mathbf{F}(t) \times \mathbf{\Omega}(\mathbf{k}), \tag{48}$$

where **F** is the electric field and  $\mathcal{E}(k)$  the band structure. Compared with Eq. (1), the last term containing the Berry curvature  $\Omega$  is new in Eq. (48). It is sometimes called the anomalous velocity and provides an anomalous contribution to the Hall current (Gradhand et al., 2012; Wimmer et al., 2017). From this term we can also see that the Berry curvature naturally defines a momentum space magnetic field (Price et al., 2014; Wimmer et al., 2017) or, put another way, the Berry curvature acts like an artificial out-of-plane magnetic field (Liu et al., 2017a).

The Berry phase and curvature play major roles not only in the various Hall effects (Fang et al., 2003; Nagaosa et al., 2010; Taguchi et al., 2001) but are also relevant to topological insulators and many other fundamental aspects of condensed matter (Chang and Niu, 1995, 1996; King-Smith and Vanderbilt, 1993; Resta, 1994; Thonhauser et al., 2005; Wilczek and Shapere, 1989; Xiao et al., 2005, 2010) and other branches of physics (Bliokh et al., 2008). However, experimental measurement of the Berry curvature remains difficult and had been restricted to optical lattices (Duca et al., 2015; Fläschner et al., 2016) until HHG in solids opened an alternative path to accessing this quantity (Luu and Wörner, 2018). In solids with broken inversion symmetry, which gives rise to a nonvanishing Berry curvature, high harmonic light parallel to the driving electric field F(t) is associated with the term  $d\mathcal{E}/d\mathbf{k}$  and high harmonic light perpendicular to the driving field is associated with the term  $e\mathbf{F}(t) \times \Omega(\mathbf{k})$  in Eq. (48).

Note that although Eq. (48) is the extension (including the Berry phase) of the equations we used for the semiclassical considerations of the intraband contributions, the effect of the Berry curvature is not restricted to the intraband mechanism. This was made clear in Chacón et al. (2020) and Jia et al. (2020) where the effect of the Berry curvature on HHG in the interband

mechanism is discussed that go beyond the pure intraband picture that was applied in Liu et al. (2017a) and Luu and Wörner (2018) for studying the Berry phase.

The broken inversion symmetry required for a nonzero Berry curvature also leads to the production of even harmonic orders, which are polarized perpendicular to the driving field, as just discussed, if they arise from the Berry curvature. Thus, a polarization resolved measurement of the HHG spectrum of  $\alpha$ -quartz was used in Luu and Wörner (2018) to measure the Berry curvature. In some cases the broken inversion symmetry is observed in a monolayer of a material but not the bulk version of it, and therefore the Berry curvature is often discussed in the context of 2D-materials, as for example in Fig. 9 for MoS<sub>2</sub>. Using 2D-materials for HHG will be discussed in more detail in Section 3.7.

## 3.5 Extracting higher order nonlinear susceptibilities

Another piece of information about the sample properties one can extract from the emitted high harmonic light is the higher order nonlinear

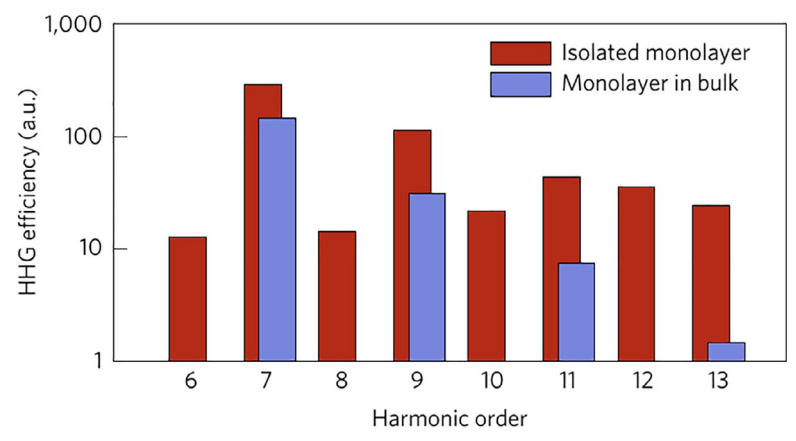


Fig. 9 Relative HHG efficiencies for an isolated monolayer and an effective monolayer in the bulk of MoS<sub>2</sub>. Strong even harmonics are observed from the isolated monolayers but are completely absent in the HHG spectrum from the bulk. The emergence of even harmonics in (isolated) monolayers is a consequence of its broken inversion symmetry, in contrast to the centrosymmetric bulk. The broken symmetry in the monolayer also gives rise to a nonvanishing Berry curvature, which leads to radiation perpendicular to the driving laser field polarization. Reprinted by permission from Springer Nature Customer Service Centre GmbH: Springer; Liu, H., Li, Y., You, Y. S., Ghimire, S., Heinz, T. F., Reis, D. A., 2017a. Highharmonic generation from an atomically thin semiconductor. Nat. Phys. 13 (3), 262–265. Copyright (2016).

susceptibility, i.e., the parameters describing the nonlinear electronic response of the material to the electric field. In Han et al. (2019) it was shown that if the high harmonic light is produced in the interband mechanism and if the transition from the valence to the conduction band happens via multiphoton absorption, leading to a perturbative scaling of the harmonic yield (i.e.,  $A \cdot I^N$  with N the harmonic order), then the prefactor A from the perturbative scaling contains all information for obtaining the nonlinear susceptibility,  $\chi^N$ , of order N.

## 3.6 Controlling HHG in solids via doping

HHG in solids is also sensitive to impurities in the material (Almalki et al., 2018; Hoang and Le, 2020; Huang et al., 2017; Jia et al., 2019; Ma et al., 2020; Mrudul et al., 2020; Pattanayak et al., 2020; Sivis et al., 2017; Yu et al., 2019a). Doping can change the electrical, magnetic, and optical characteristics of solid by changing the band structure (Huang et al., 2017), and hence also affects high harmonic emission. For instance, doping can lead to an enhanced harmonic yield of several orders of magnitude (Hoang and Le, 2020; Huang et al., 2017; Ma et al., 2020; Pattanayak et al., 2020; Yu et al., 2019a) or the cutoff and overall shape of the spectrum can be changed significantly compared to the undoped material (Pattanayak et al., 2020). In Almalki et al. (2018), tomographic reconstruction of the impurity ground state is demonstrated and the impurity dipole moment is found to be the dominant factor in determining the magnitude of the harmonic signal. Also, doping can affect symmetry properties and thus lead to the emergence of even harmonics where in the undoped counterpart only odd harmonics were observed (Jia et al., 2019). Thus, high harmonic light can serve as a tool to study the concentration and structure of impurities (Mrudul et al., 2020; Pattanayak et al., 2020) and, the other way around, doping can serve as a tool to control the high harmonic spectrum.

## 3.7 HHG in graphene and other 2D materials

Many HHG experiments in solids are conducted with monolayer 2D materials such as graphene (Al-Naib et al., 2014; Chen and Qin, 2019; Chizhova et al., 2017; Dimitrovski et al., 2017; Hafez et al., 2018; Liu et al., 2018a; Taucer et al., 2017; Yoshikawa et al., 2017; Zurrón-Cifuentes et al., 2019), hexagonal boron nitride (h-BN) (Le Breton et al., 2018; Mrudul et al., 2020; Tancogne-Dejean and Rubio, 2018; Yu et al., 2018) or transition-metal dichalcogenides (Langer et al., 2018; Liu et al., 2017a; Yoshikawa et al., 2019).

As we have already touched upon in Section 3.3, monolayer 2D materials exhibit other symmetry properties than their bulk counterpart (Molina-Sanchez and Wirtz, 2011). The symmetry breaking in a monolayer is obvious if the incident laser pulse probes electron dynamics along the out-of-plane direction, but is restricted due to the lack of lattice sites in this orientation. On a more fundamental level we can think of the bulk crystal as having, for example, a bilayer unit cell (e.g., in the case of MoS<sub>2</sub>) and therefore taking only a monolayer breaks the inversion symmetry (Kang et al., 2015; Liu et al., 2017a; Molina-Sanchez and Wirtz, 2011).

Another crucial difference between HHG from a bulk or 2D monolayer is that pulse propagation effects, such as phase matching, can be neglected in the monolayer (Yoshikawa et al., 2017; Yue and Gaarde, 2020a). Also, in Tancogne-Dejean and Rubio (2018), Le Breton et al. (2018), and Liu et al. (2017a) HHG from monolayers and their corresponding bulk crystals was studied, comparing the atomic and bulk characteristics of the emitted light. In Liu et al. (2017a) it was shown for MoS<sub>2</sub> that HHG from a monolayer is more efficient than from its bulk counterpart. And in Tancogne-Dejean and Rubio (2018) it was demonstrated that h-BN monolayers lead to HHG similar to HHG in atoms or in the bulk, depending on the orientation of the incident light.

One 2D material that has attracted special attention is graphene. It has a zero energy gap and a linear energy dispersion that corresponds to an effective electron and hole mass of zero (Yoshikawa et al., 2017). The generation of high harmonics from this special material has been investigated intensely in the past few years, both theoretically (Al-Naib et al., 2014, 2015; Avetissian and Mkrtchian, 2018; Avetissian et al., 2012a,b, 2020; Boyero-García et al., 2019; Chen and Qin, 2019; Chizhova et al., 2016, 2017; Cox et al., 2017; Dimitrovski et al., 2017; Ghazaryan et al., 2020; Ishikawa, 2010; Liu et al., 2018a; Mikhailov, 2007; Mikhailov and Ziegler, 2008; Mrudul et al., 2021; Sørngård et al., 2013; Zurrón-Cifuentes et al., 2019) and experimentally (Baudisch et al., 2018; Bowlan et al., 2014a,b; Hafez et al., 2018; Taucer et al., 2017; Yoshikawa et al., 2017). The linear dispersion relation is expected to lead to strong nonlinear optical effects. However, the maximum harmonic order produced experimentally is the ninth harmonic (Chen and Qin, 2019; Yoshikawa et al., 2017).

Another interesting effect of HHG in graphene is its ellipticity dependence, for which a variety of disparate results have been found. Experimentally, Taucer et al. (2017) and Baudisch et al. (2018) find the largest HHG yield when the driving laser field is linearly polarized, with a monotonic decrease of the HHG yield as the ellipticity grows. A decrease in HHG with increasing

ellipticity is also observed in the gas phase. Yoshikawa et al. (2017), by contrast, measure a maximum HHG yield not for linearly polarized light but for an ellipticity of  $\varepsilon=0.32$ . This local maximum was explained in Liu et al. (2018a), where it was shown theoretically that the interband and intraband contributions exhibit a different ellipticity dependence, with the interband mechanism giving a maximum yield at a nonzero ellipticity if the dephasing time was chosen such that best agreement with the experimental results of Yoshikawa et al. (2017) is obtained.

Also, not only the yield but also the polarization of the resulting high harmonic light was observed to have a strong ellipticity dependence in theoretical studies. In Zurrón-Cifuentes et al. (2019), for instance, it is claimed that linearly polarized driving fields in graphene can result in the emission of elliptically polarized harmonics, and that elliptically polarized driving fields may result in linearly polarized or ellipticity reversed harmonics.

The study of HHG from 2D materials may also be relevant for technological applications. For example, the insights that the emitted high harmonics allow into light-driven electron dynamics may be relevant for valleytronics (Schaibley et al., 2016). Local minima in the conduction band and local maxima in the valence band are so called valleys, and the electron occupation of a certain valley presents an additional degree of freedom to store and carry information (Schaibley et al., 2016). Two inequivalent valleys, such as they occur at the *K* and *K'* points in graphene or transition metal dichalcogenides, are material characteristics that valleytronics relies on. It has, for instance, been shown that the subcycle change of the valley polarization is encoded in the high-odd-order sidebands of the spectrum (Langer et al., 2018) or that the valley pseudospin can be mapped onto the polarization structure of the emitted harmonics (Jiménez-Galán et al., 2020, 2021).

# 4. Conclusion and outlook

In this review, we have looked at the burgeoning field of high-harmonic generation from solids. We have discussed similarities and differences to high-harmonic generation in the gas phase, as well as highlighted the many new opportunities and open questions that HHG in solids offers. Besides being an important new light source, HHG in solids offers new ways to study light-matter interaction and extract information about nonlinear electronic response in condensed matter systems.

At the end of this review we want to emphasize that high-harmonic generation is a rapidly evolving field and there are many aspects that were not covered here. For example, nanostructuring the irradiated sample opens many new options for spatially confining and enhancing the driving field (Han et al., 2016; Liu et al., 2018b; Sivis et al., 2017; Vampa et al., 2017). The local enhancement of the field near a nanostructure can result in the enhancement of the HHG yield (Liu et al., 2018b; Vampa et al., 2017). Enhancement of the HHG production efficiency was also achieved by using a periodic array of thin one-dimensional crystalline silicon ridge waveguides, where the vacuum gaps between the ridges reduce the high re-absorption loss of the bulk (Liu et al., 2020). Moreover, nanostructuring the irradiated sample allows to tailor the structure of the emitted highharmonic light, for example its polarization or potentially also the orbital angular momentum (Vampa et al., 2017). Thus, combining the fields of nanostructuring and high-harmonic generation promises applications of attosecond physics in optoelectronics (Liu et al., 2018b, 2020; Sivis et al., 2017; Vampa et al., 2017).

Another aspect we have neglected are correlation effects. We assumed an independent electron approximation, which in many cases is indeed sufficient to explain key observations in conventional semiconductors (Imai et al., 2020). In Hansen et al. (2017), for instance, the result from full TDDFT simulations, which include electron-electron interaction on a mean-field level, with results from simulations with frozen Kohn-Sham potentials, it was found that the dynamic electron-electron interaction is of minor relevance in typically studied HHG systems. A similar result was found in Tancogne-Dejean et al. (2017b). However, there are also studies that indicate the relevance of taking into account the interaction between electrons (or electron-hole pairs) (Ikemachi et al., 2018; Liu and Bian, 2020). Going beyond conventional semiconductors and generating high-harmonics in strongly correlated materials shows a rich physics of nonequilibrium many-body dynamics that is imprinted in the emitted high harmonic light (Imai et al., 2020; Murakami et al., 2018; Silva et al., 2018).

These examples of nanostructuring and correlation effects, along with the applications of HHG in solids mentioned in the main text, make clear that HHG in solids is an exciting new field of research that promises to lead to new insights about light-matter interaction and to new applications in e.g., the optoelectronics domain.

Finally, it seems clear that there is still a plethora of open questions. The ongoing debate about the underlying mechanism of HHG in solids, interband

versus intraband, that we looked at in Section 2.7, is a case in point. These questions still need to be resolved to harness the full potential of high-harmonic generation in solids.

## Acknowledgments

L.O. was supported by the Center for Emergent Materials, an NSF-funded MRSEC, under Grant No. DMR-2011876.

#### References

- Al-Naib, I., Sipe, J.E., Dignam, M.M., 2014. High harmonic generation in undoped graphene: interplay of inter-and intraband dynamics. Phys. Rev. B 90 (24), 245423.
- Al-Naib, I., Sipe, J.E., Dignam, M.M., 2015. Nonperturbative model of harmonic generation in undoped graphene in the terahertz regime. New J. Phys. 17 (11), 113018.
- Almalki, S., 2019. Nano-Engineering of High Harmonic Generation in Solid State Systems. Ph.D. thesis, Université d'Ottawa/University of Ottawa.
- Almalki, S., Parks, A.M., Bart, G., Corkum, P.B., Brabec, T., McDonald, C.R., 2018. High harmonic generation tomography of impurities in solids: conceptual analysis. Phys. Rev. B 98 (14), 144307.
- Alon, O.E., Averbukh, V., Moiseyev, N., 1998. Selection rules for the high harmonic generation spectra. Phys. Rev. Lett. 80 (17), 3743.
- Amini, K., Biegert, J., Calegari, F., Chacón, A., Ciappina, M.F., Dauphin, A., Efimov, D.K., de Morisson Faria, C.F., Giergiel, K., Gniewek, P., et al., 2019. Symphony on strong field approximation. Rep. Prog. Phys. 82 (11), 116001.
- Ashcroft, N.W., Mermin, N.D., et al., 1976. Solid State Physics. Holt, Rinehart and Winston, New York.
- Avetissian, H.K., Mkrtchian, G.F., 2018. Impact of electron-electron Coulomb interaction on the high harmonic generation process in graphene. Phys. Rev. B 97 (11), 115454.
- Avetissian, H.K., Avetissian, A.K., Mkrtchian, G.F., Sedrakian, K.V., 2012a. Creation of particle-hole superposition states in graphene at multiphoton resonant excitation by laser radiation. Phys. Rev. B 85 (11), 115443.
- Avetissian, H.K., Avetissian, A.K., Mkrtchian, G.F., Sedrakian, K.V., 2012b. Multiphoton resonant excitation of Fermi-Dirac sea in graphene at the interaction with strong laser fields. J. Nanophotonics 6 (1), 061702.
- Avetissian, H.K., Avetissian, A.K., Ghazaryan, A.G., Mkrtchian, G.F., Sedrakian, K.V., 2020. High-harmonic generation at particle-hole multiphoton excitation in gapped bilayer graphene. J. Nanophotonics 14 (2), 026004.
- Baudisch, M., Marini, A., Cox, J.D., Zhu, T., Silva, F., Teichmann, S., Massicotte, M., Koppens, F., Levitov, L.S., de Abajo, F.J.G., et al., 2018. Ultrafast nonlinear optical response of Dirac fermions in graphene. Nat. Commun. 9 (1), 1–6.
- Berry, M.V., 1984. Quantal phase factors accompanying adiabatic changes. Proc. R. Soc. Lond. A Math. Phys. Sci. 392 (1802), 45–57.
- Bliokh, K.Y., Niv, A., Kleiner, V., Hasman, E., 2008. Geometrodynamics of spinning light. Nat. Photonics 2 (12), 748.
- Bloch, F., 1929. Über die quantenmechanik der elektronen in kristallgittern. Z. Phys. 52 (7–8), 555–600.
- Bowlan, P., Martinez-Moreno, E., Reimann, K., Elsaesser, T., Woerner, M., 2014a. Ultrafast terahertz response of multilayer graphene in the nonperturbative regime. Phys. Rev. B 89 (4), 041408.

- Bowlan, P., Martinez-Moreno, E., Reimann, K., Woerner, M., Elsaesser, T., 2014b. Terahertz radiative coupling and damping in multilayer graphene. New J. Phys. 16 (1), 013027.
- Boyero-García, R., Zurrón-Cifuentes, O., Hernández-García, C., Picón, A., Plaja, L., 2019. Polarization control of high-harmonic pulses generated in gapless graphene. In: The European Conference on Lasers and Electro-Optics, Optical Society of America, p. cg\_p\_31.
- Budil, K.S., Salières, P., L'Huillier, A., Ditmire, T., Perry, M.D., 1993. Influence of ellipticity on harmonic generation. Phys. Rev. A 48 (5), R3437.
- Burnett, N.H., Kan, C., Corkum, P.B., 1995. Ellipticity and polarization effects in harmonic generation in ionizing neon. Phys. Rev. A 51 (5), R3418.
- Chacón, A., Kim, D., Zhu, W., Kelly, S.P., Dauphin, A., Pisanty, E., Maxwell, A.S., Picón, A., Ciappina, M.F., Kim, D.E., et al., 2020. Circular dichroism in higher-order harmonic generation: heralding topological phases and transitions in Chern insulators. Phys. Rev. B 102 (13), 134115.
- Chang, M.-C., Niu, Q., 1995. Berry phase, hyperorbits, and the Hofstadter spectrum. Phys. Rev. Lett. 75 (7), 1348.
- Chang, M.-C., Niu, Q., 1996. Berry phase, hyperorbits, and the Hofstadter spectrum: semi-classical dynamics in magnetic Bloch bands. Phys. Rev. B 53 (11), 7010.
- Chen, Z.-Y., Qin, R., 2019. Circularly polarized extreme ultraviolet high harmonic generation in graphene. Opt. Express 27 (3), 3761–3770.
- Cheng, B., Kanda, N., Ikeda, T.N., Matsuda, T., Xia, P., Schumann, T., Stemmer, S., Itatani, J., Armitage, N.P., Matsunaga, R., 2020. Efficient terahertz harmonic generation with coherent acceleration of electrons in the Dirac semimetal Cd<sub>3</sub>As<sub>2</sub>. Phys. Rev. Lett. 124 (11), 117402.
- Chizhova, L.A., Libisch, F., Burgdörfer, J., 2016. Nonlinear response of graphene to a few-cycle terahertz laser pulse: role of doping and disorder. Phys. Rev. B 94 (7), 075412.
- Chizhova, L.A., Libisch, F., Burgdörfer, J., 2017. High-harmonic generation in graphene: interband response and the harmonic cutoff. Phys. Rev. B 95 (8), 085436.
- Constant, E., Garzella, D., Breger, P., Mével, E., Dorrer, C., Le Blanc, C., Salin, F., Agostini, P., 1999. Optimizing high harmonic generation in absorbing gases: model and experiment. Phys. Rev. Lett. 82 (8), 1668.
- Corkum, P.B., 1993. Plasma perspective on strong field multiphoton ionization. Phys. Rev. Lett. 71 (13), 1994.
- Cox, J.D., Marini, A., De Abajo, F.J.G., 2017. Plasmon-assisted high-harmonic generation in graphene. Nat. Commun. 8 (1), 1–7.
- Dachraoui, H., Auguste, T., Helmstedt, A., Bartz, P., Michelswirth, M., Mueller, N., Pfeiffer, W., Salieres, P., Heinzmann, U., 2009. Interplay between absorption, dispersion and refraction in high-order harmonic generation. J. Phys. B At. Mol. Opt. Phys. 42 (17), 175402.
- Damascelli, A., Hussain, Z., Shen, Z.-X., 2003. Angle-resolved photoemission studies of the cuprate superconductors. Rev. Mod. Phys. 75 (2), 473.
- DiChiara, A.D., Sistrunk, E., Miller, T.A., Agostini, P., DiMauro, L.F., 2009. An investigation of harmonic generation in liquid media with a mid-infrared laser. Opt. Express 17 (23), 20959–20965.
- Dimitrovski, D., Madsen, L.B., Pedersen, T.G., 2017. High-order harmonic generation from gapped graphene: perturbative response and transition to nonperturbative regime. Phys. Rev. B 95 (3), 035405.
- Du, T.-Y., 2019. Probing the dephasing time of crystals via spectral properties of high-order harmonic generation. Phys. Rev. A 100 (5), 053401.
- Du, T.-Y., Bian, X.-B., 2017. Quasi-classical analysis of the dynamics of the high-order harmonic generation from solids. Opt. Express 25 (1), 151–158.

- Du, T.-Y., Guan, Z., Zhou, X.-X., Bian, X.-B., 2016. Enhanced high-order harmonic generation from periodic potentials in inhomogeneous laser fields. Phys. Rev. A 94 (2), 023419.
- Du, T.-Y., Tang, D., Bian, X.-B., 2018. Subcycle interference in high-order harmonic generation from solids. Phys. Rev. A 98 (6), 063416.
- Duca, L., Li, T., Reitter, M., Bloch, I., Schleier-Smith, M., Schneider, U., 2015. An Aharonov-Bohm interferometer for determining Bloch band topology. Science 347 (6219), 288–292.
- Ernotte, G., Taucer, M., Corkum, P.B., 2019. A Wannier perspective on high harmonic generation in solids. In: Laser Sci, Optical Society of America. JW4A–26.
- Faisal, F.H.M., 1973. Multiple absorption of laser photons by atoms. J. Phys. B At. Mol. Phys. 6 (4), L89.
- Fang, Z., Nagaosa, N., Takahashi, K.S., Asamitsu, A., Mathieu, R., Ogasawara, T., Yamada, H., Kawasaki, M., Tokura, Y., Terakura, K., 2003. The anomalous Hall effect and magnetic monopoles in momentum space. Science 302 (5642), 92–95.
- Feise, M.W., Citrin, D.S., 1999. Semiclassical theory of terahertz multiple-harmonic generation in semiconductor superlattices. Appl. Phys. Lett. 75 (22), 3536–3538.
- Fläschner, N., Rem, B.S., Tarnowski, M., Vogel, D., Lühmann, D.S., Sengstock, K., Weitenberg, C., 2016. Experimental reconstruction of the Berry curvature in a Floquet Bloch band. Science 352 (6289), 1091–1094.
- Floss, I., Lemell, C., Wachter, G., Smejkal, V., Sato, S.A., Tong, X.-M., Yabana, K., Burgdörfer, J., 2018. Ab initio multiscale simulation of high-order harmonic generation in solids. Phys. Rev. A 97 (1), 011401.
- Floss, I., Lemell, C., Yabana, K., Burgdörfer, J., 2019. Incorporating decoherence into solid-state time-dependent density functional theory. Phys. Rev. B 99 (22), 224301.
- Földi, P., 2017. Gauge invariance and interpretation of interband and intraband processes in high-order harmonic generation from bulk solids. Phys. Rev. B 96 (3), 035112.
- Földi, P., Benedict, M.G., Yakovlev, V.S., 2013. The effect of dynamical Bloch oscillations on optical-field-induced current in a wide-gap dielectric. New J. Phys. 15 (6), 063019.
- Garg, M., Zhan, M., Luu, T.T., Lakhotia, H., Klostermann, T., Guggenmos, A., Goulielmakis, E., 2016. Multi-petahertz electronic metrology. Nature 538 (7625), 359–363.
- Ghazaryan, A.G., Matevosyan, H.H., Sedrakian, K.V., 2020. High harmonics generation in bilayer graphene at high Fermi energies induced by coherent THz-radiation. J. Nanophotonics 14 (4), 046009.
- Ghimire, S., Reis, D.A., 2019. High-harmonic generation from solids. Nat. Phys. 15 (1), 10–16.
- Ghimire, S., DiChiara, A.D., Sistrunk, E., Agostini, P., DiMauro, L.F., Reis, D.A., 2011. Observation of high-order harmonic generation in a bulk crystal. Nat. Phys. 7 (2), 138–141.
- Ghimire, S., DiChiara, A.D., Sistrunk, E., Ndabashimiye, G., Szafruga, U.B., Mohammad, A., Agostini, P., DiMauro, L.F., Reis, D.A., 2012a. Generation and propagation of high-order harmonics in crystals. Phys. Rev. A 85 (4), 043836.
- Ghimire, S., Ndabashimiye, G., Reis, D.A., 2012b. High-order harmonic generation in solid argon. In: Quantum Electronics and Laser Science Conference, Optical Society of America. QW1F–1.
- Ghimire, S., Ndabashimiye, G., DiChiara, A.D., Sistrunk, E., Stockman, M.I., Agostini, P., DiMauro, L.F., Reis, D.A., 2014. Strong-field and attosecond physics in solids. J. Phys. B At. Mol. Opt. Phys. 47 (20), 204030.
- Golde, D., Meier, T., Koch, S.W., 2008. High harmonics generated in semiconductor nanostructures by the coupled dynamics of optical inter-and intraband excitations. Phys. Rev. B 77 (7), 075330.

- Gradhand, M., Fedorov, D.V., Pientka, F., Zahn, P., Mertig, I., Györffy, B.L., 2012. First-principle calculations of the Berry curvature of Bloch states for charge and spin transport of electrons. J. Phys. Condens. Matter 24 (21), 213202.
- Guan, Z., Zhou, X.-X., Bian, X.-B., 2016. High-order-harmonic generation from periodic potentials driven by few-cycle laser pulses. Phys. Rev. A 93 (3), 033852.
- Guan, M.-X., Lian, C., Hu, S.-Q., Liu, H., Zhang, S.-J., Zhang, J., Meng, S., 2019. Cooperative evolution of intraband and interband excitations for high-harmonic generation in strained MoS 2. Phys. Rev. B 99 (18), 184306.
- Hafez, H.A., Kovalev, S., Deinert, J.-C., Mics, Z., Green, B., Awari, N., Chen, M., Germanskiy, S., Lehnert, U., Teichert, J., et al., 2018. Extremely efficient terahertz high-harmonic generation in graphene by hot Dirac fermions. Nature 561 (7724), 507–511.
- Han, S., Kim, H., Kim, Y.W., Kim, Y.-J., Kim, S., Park, I.-Y., Kim, S.-W., 2016. High-harmonic generation by field enhanced femtosecond pulses in metal-sapphire nanostructure. Nat. Commun. 7 (1), 1–7.
- Han, S., Ortmann, L., Kim, H., Kim, Y.W., Oka, T., Chacon, A., Doran, B., Ciappina, M., Lewenstein, M., Kim, S.-W., et al., 2019. Extraction of higher-order nonlinear electronic response in solids using high harmonic generation. Nat. Commun. 10 (1), 1–6.
- Hansen, K.K., Deffge, T., Bauer, D., 2017. High-order harmonic generation in solid slabs beyond the single-active-electron approximation. Phys. Rev. A 96 (5), 053418.
- Hansen, K.K., Bauer, D., Madsen, L.B., 2018. Finite-system effects on high-harmonic generation: from atoms to solids. Phys. Rev. A 97, 043424.
- Haug, H., Koch, S.W., 2015. Quantum Theory of the Optical and Electronic Properties of Semiconductors, fifth ed. World Scientific Publishing Company.
- Hawkins, P.G., Ivanov, M.Y., Yakovlev, V.S., 2015. Effect of multiple conduction bands on high-harmonic emission from dielectrics. Phys. Rev. A 91 (1), 013405.
- Heissler, P., Lugovoy, E., Hörlein, R., Waldecker, L., Wenz, J., Heigoldt, M., Khrennikov, K., Karsch, S., Krausz, F., Abel, B., et al., 2014. Using the third state of matter: high harmonic generation from liquid targets. New J. Phys. 16 (11), 113045.
- Higuchi, T., Stockman, M.I., Hommelhoff, P., 2014. Strong-field perspective on high-harmonic radiation from bulk solids. Phys. Rev. Lett. 113 (21), 213901.
- Hirori, H., Xia, P., Shinohara, Y., Otobe, T., Sanari, Y., Tahara, H., Ishii, N., Itatani, J., Ishikawa, K.L., Aharen, T., et al., 2019. High-order harmonic generation from hybrid organic-inorganic perovskite thin films. APL Materials 7 (4), 041107.
- Hoang, V.-H., Le, A.-T., 2020. Factorization of high-order-harmonic-generation yields in impurity-doped materials. Phys. Rev. A 102 (2), 023112.
- Hofmann, P., 2014. Online note on Bloch oscillations to accompany the book solid state physics—an introduction, Wiley VCH. accessed September 15, 2020 https://philiphofmann.net/solid-state-physics-book/solid-state-notes/.
- Hofmann, P., 2015. Solid State Physics: An Introduction. John Wiley & Sons.
- Hohenleutner, M., Langer, F., Schubert, O., Knorr, M., Huttner, U., Koch, S.W., Kira, M., Huber, R., 2015. Real-time observation of interfering crystal electrons in high-harmonic generation. Nature 523 (7562), 572–575.
- Huang, T., Zhu, X., Li, L., Liu, X., Lan, P., Lu, P., 2017. High-order-harmonic generation of a doped semiconductor. Phys. Rev. A 96 (4), 043425.
- Huttner, U., Schuh, K., Moloney, J.V., Koch, S.W., 2016. Similarities and differences between high-harmonic generation in atoms and solids. JOSA B 33 (7), C22–C29.
- Ikemachi, T., Shinohara, Y., Sato, T., Yumoto, J., Kuwata-Gonokami, M., Ishikawa, K.L., 2017. Trajectory analysis of high-order-harmonic generation from periodic crystals. Phys. Rev. A 95 (4), 043416.
- Ikemachi, T., Shinohara, Y., Sato, T., Yumoto, J., Kuwata-Gonokami, M., Ishikawa, K.L., 2018. Time-dependent Hartree-Fock study of electron-hole interaction effects on high-order harmonic generation from periodic crystals. Phys. Rev. A 98 (2), 023415.

- Imai, S., Ono, A., Ishihara, S., 2020. High harmonic generation in a correlated electron system. Phys. Rev. Lett. 124 (15), 157404.
- Ishikawa, K.L., 2010. Nonlinear optical response of graphene in time domain. Phys. Rev. B 82 (20), 201402.
- Ivanov, M., Smirnova, O., 2013. Opportunities for sub-laser-cycle spectroscopy in condensed phase. Chem. Phys. 414, 3–9.
- Ivanov, M.Y., Spanner, M., Smirnova, O., 2005. Anatomy of strong field ionization. J. Mod. Opt. 52 (2–3), 165–184.
- Jia, G.-R., Huang, X.-H., Bian, X.-B., 2017. Nonadiabatic redshifts in high-order harmonic generation from solids. Opt. Express 25 (20), 23654–23662.
- Jia, L., Zhang, Z., Yang, D.Z., Si, M.S., Zhang, G.P., Liu, Y.S., 2019. High harmonic generation in magnetically-doped topological insulators. Phys. Rev. B 100 (12), 125144.
- Jia, L., Zhang, Z., Yang, D.Z., Liu, Y., Si, M.S., Zhang, G.P., Liu, Y.S., 2020. Optical high-order harmonic generation as a structural characterization tool. Phys. Rev. B 101 (14), 144304.
- Jiang, S., Gholam-Mirzaei, S., Crites, E., Beetar, J.E., Singh, M., Lu, R., Chini, M., Lin, C.D., 2019. Crystal symmetry and polarization of high-order harmonics in ZnO. J. Phys. B At. Mol. Opt. Phys. 52 (22), 225601.
- Jiménez-Galán, Á., Silva, R.E.F., Smirnova, O., Ivanov, M., 2020. Lightwave control of topological properties in 2D materials for sub-cycle and non-resonant valley manipulation. Nat. Photonics 14 (12), 728–732.
- Jiménez-Galán, A., Silva, R., Smirnova, O., Ivanov, M., 2021. Sub-cycle valleytronics: control of valley polarization using few-cycle linearly polarized pulses. Optica 8 (3), 277–280.
- Jin, J.-Z., Xiao, X.-R., Liang, H., Wang, M.-X., Chen, S.-G., Gong, Q., Peng, L.-Y., 2018. High-order harmonic generation from a two-dimensional band structure. Phys. Rev. A 97 (4), 043420.
- Jürgens, P., Liewehr, B., Kruse, B., Peltz, C., Engel, D., Husakou, A., Witting, T., Ivanov, M., Vrakking, M.J.J., Fennel, T., et al., 2020. Origin of strong-field-induced low-order harmonic generation in amorphous quartz. Nat. Phys. 16 (10), 1035–1039.
- Jürß, C., Bauer, D., 2019. High-harmonic generation in Su-Schrieffer-Heeger chains. Phys. Rev. B 99 (19), 195428.
- Kaneshima, K., Shinohara, Y., Takeuchi, K., Ishii, N., Imasaka, K., Kaji, T., Ashihara, S., Ishikawa, K.L., Itatani, J., 2018. Polarization-resolved study of high harmonics from bulk semiconductors. Phys. Rev. Lett. 120 (24), 243903.
- Kang, J., Sahin, H., Peeters, F.M., 2015. Mechanical properties of monolayer sulphides: a comparative study between MoS<sub>2</sub>, HfS<sub>2</sub> and TiS<sub>3</sub>. Phys. Chem. Chem. Phys. 17 (41), 27742–27749.
- Kazamias, S., Douillet, D., Weihe, F., Valentin, C., Rousse, A., Sebban, S., Grillon, G., Augé, F., Hulin, D., Balcou, P., 2003. Global optimization of high harmonic generation. Phys. Rev. Lett. 90 (19), 193901.
- Keldysh, L.V., 1965. Ionization in the field of a strong electromagnetic wave. Sov. Phys. JETP 20, 1307.
- Kilen, I., Kolesik, M., Hader, J., Moloney, J.V., Huttner, U., Hagen, M.K., Koch, S.W., 2020. Propagation induced dephasing in semiconductor high-harmonic generation. Phys. Rev. Lett. 125 (8), 083901.
- Kim, Y.W., Shao, T.-J., Kim, H., Han, S., Kim, S., Ciappina, M., Bian, X.-B., Kim, S.-W., 2019. Spectral interference in high harmonic generation from solids. ACS Photonics 6 (4), 851–857.
- King-Smith, R.D., Vanderbilt, D., 1993. Theory of polarization of crystalline solids. Phys. Rev. B 47 (3), 1651.

- Kogar, A., 2016. Wannier-stark ladder, wavefunction localization and Bloch oscillations. [accessed September 8, 2020] https://thiscondensedlife.wordpress.com/2016/12/01/wannier-stark-ladder-wavefunction-localization-and-bloch-oscillations/.
- Kopold, R., Milošević, D.B., Becker, W., 2000. Rescattering processes for elliptical polarization: a quantum trajectory analysis. Phys. Rev. Lett. 84 (17), 3831.
- Krasikov, I., 2006. Uniform bounds for Bessel functions. J. Appl. Anal. 12 (1), 83-91.
- Krause, J.L., Schafer, K.J., Kulander, K.C., 1992. High-order harmonic generation from atoms and ions in the high intensity regime. Phys. Rev. Lett. 68 (24), 3535.
- Krausz, F., Ivanov, M., 2009. Attosecond physics. Rev. Mod. Phys. 81 (1), 163.
- Kruchinin, S.Y., Krausz, F., Yakovlev, V.S., 2018. Colloquium: strong-field phenomena in periodic systems. Rev. Mod. Phys. 90 (2), 021002.
- Landau, L.J., 2000. Bessel functions: monotonicity and bounds. J. Lond. Math. Soc. 61 (1), 197–215.
- Langer, F., Hohenleutner, M., Schmid, C.P., Pöllmann, C., Nagler, P., Korn, T., Schüller, C., Sherwin, M.S., Huttner, U., Steiner, J.T., et al., 2016. Lightwave-driven quasiparticle collisions on a subcycle timescale. Nature 533 (7602), 225–229.
- Langer, F., Hohenleutner, M., Huttner, U., Koch, S.W., Kira, M., Huber, R., 2017. Symmetry-controlled temporal structure of high-harmonic carrier fields from a bulk crystal. Nat. Photonics 11 (4), 227–231.
- Langer, F., Schmid, C.P., Schlauderer, S., Gmitra, M., Fabian, J., Nagler, P., Schüller, C., Korn, T., Hawkins, P.G., Steiner, J.T., et al., 2018. Lightwave valleytronics in a monolayer of tungsten diselenide. Nature 557 (7703), 76–80.
- Lanin, A.A., Stepanov, E.A., Fedotov, A.B., Zheltikov, A.M., 2017. Mapping the electron band structure by intraband high-harmonic generation in solids. Optica 4 (5), 516–519.
- Le Breton, G., Rubio, A., Tancogne-Dejean, N., 2018. High-harmonic generation from few-layer hexagonal boron nitride: evolution from monolayer to bulk response. Phys. Rev. B 98 (16), 165308.
- Lewenstein, M., Balcou, P., Ivanov, M.Y., L'huillier, A., Corkum, P.B., 1994. Theory of high-harmonic generation by low-frequency laser fields. Phys. Rev. A 49 (3), 2117.
- Li, J., Zhang, Q., Li, L., Zhu, X., Huang, T., Lan, P., Lu, P., 2019a. Orientation dependence of high-order harmonic generation in nanowire. Phys. Rev. A 99 (3), 033421.
- Li, L., Lan, P., Zhu, X., Huang, T., Zhang, Q., Lein, M., Lu, P., 2019b. Reciprocal-space-trajectory perspective on high-harmonic generation in solids. Phys. Rev. Lett. 122 (19), 193901.
- Li, J., Lu, J., Chew, A., Han, S., Li, J., Wu, Y., Wang, H., Ghimire, S., Chang, Z., 2020. Attosecond science based on high harmonic generation from gases and solids. Nat. Commun. 11 (1), 1–13.
- Liu, J.-Q., Bian, X.-B., 2020. Effect of electron-electron interactions on high-order harmonic generation in crystals. Phys. Rev. B 102 (17), 174302.
- Liu, H., Li, Y., You, Y.S., Ghimire, S., Heinz, T.F., Reis, D.A., 2017a. High-harmonic generation from an atomically thin semiconductor. Nat. Phys. 13 (3), 262–265.
- Liu, X., Zhu, X., Lan, P., Zhang, X., Wang, D., Zhang, Q., Lu, P., 2017b. Time-dependent population imaging for high-order-harmonic generation in solids. Phys. Rev. A 95 (6), 063419.
- Liu, X., Zhu, X., Zhang, X., Wang, D., Lan, P., Lu, P., 2017c. Wavelength scaling of the cutoff energy in the solid high harmonic generation. Opt. Express 25 (23), 29216–29224.
- Liu, C., Zheng, Y., Zeng, Z., Li, R., 2018a. Driving-laser ellipticity dependence of high-order harmonic generation in graphene. Phys. Rev. A 97 (6), 063412.
- Liu, H., Guo, C., Vampa, G., Zhang, J.L., Sarmiento, T., Xiao, M., Bucksbaum, P.H., Vučković, J., Fan, S., Reis, D.A., 2018b. Enhanced high-harmonic generation from an all-dielectric metasurface. Nat. Phys. 14 (10), 1006–1010.

- Liu, H., Vampa, G., Zhang, J.L., Shi, Y., Buddhiraju, S., Fan, S., Vuckovic, J., Bucksbaum, P.H., Reis, D.A., 2020. Beating absorption in solid-state high harmonics. Commun. Phys. 3 (1), 1–6.
- Lu, J., Cunningham, E.F., You, Y.S., Reis, D.A., Ghimire, S., 2019. Interferometry of dipole phase in high harmonics from solids. Nat. Photonics 13 (2), 96–100.
- Luu, T.T., Wörner, H.J., 2016. High-order harmonic generation in solids: a unifying approach. Phys. Rev. B 94 (11), 115164.
- Luu, T.T., Wörner, H.J., 2018. Measurement of the Berry curvature of solids using high-harmonic spectroscopy. Nat. Commun. 9 (1), 1–6.
- Luu, T.T., Garg, M., Kruchinin, S.Y., Moulet, A., Hassan, M.T., Goulielmakis, E., 2015. Extreme ultraviolet high-harmonic spectroscopy of solids. Nature 521 (7553), 498–502.
- Luu, T.T., Yin, Z., Jain, A., Gaumnitz, T., Pertot, Y., Ma, J., Wörner, H.J., 2018. Extreme-ultraviolet high-harmonic generation in liquids. Nat. Commun. 9 (1), 1–10.
- Ma, J., Zhang, C., Cui, H., Ma, Z., Miao, X., 2020. Theoretical investigation of the electron dynamics in high-order harmonic generation process from the doped periodic potential. Chem. Phys. Lett. 744, 137207.
- McDonald, C.R., Vampa, G., Corkum, P.B., Brabec, T., 2015a. Interband Bloch oscillation mechanism for high-harmonic generation in semiconductor crystals. Phys. Rev. A 92 (3), 033845.
- McDonald, C.R., Vampa, G., Orlando, G., Corkum, P.B., Brabec, T., 2015b. Theory of high-harmonic generation in solids. IOP J. Phys. Conf. Ser. 594, 012021.
- McDonald, C.R., Amin, K.S., Aalmalki, S., Brabec, T., 2017. Enhancing high harmonic output in solids through quantum confinement. Phys. Rev. Lett. 119 (18), 183902.
- Mikhailov, S.A., 2007. Non-linear electromagnetic response of graphene. EPL 79 (2), 27002.
- Mikhailov, S.A., Ziegler, K., 2008. Nonlinear electromagnetic response of graphene: frequency multiplication and the self-consistent-field effects. J. Phys. Condens. Matter 20 (38), 384204.
- Molina-Sanchez, A., Wirtz, L., 2011. Phonons in single-layer and few-layer MoS 2 and WS 2. Phys. Rev. B 84 (15), 155413.
- Mrudul, M.S., Jiménez-Galán, A., Ivanov, M., Dixit, G., 2021. Light-induced valleytronics in pristine graphene. Optica 8 (3), 422–427.
- Mrudul, M., Pattanayak, A., Ivanov, M., Dixit, G., et al., 2019. Direct numerical observation of real-space recollision in high-order harmonic generation from solids. Phys. Rev. A 100 (4), 043420.
- Mrudul, M.S., Tancogne-Dejean, N., Rubio, A., Dixit, G., 2020. High-harmonic generation from spin-polarised defects in solids. npj Comput. Mater. 6 (1), 1–9.
- Mücke, O.D., 2011. Isolated high-order harmonics pulse from two-color-driven Bloch oscillations in bulk semiconductors. Phys. Rev. B 84 (8), 081202.
- Murakami, Y., Eckstein, M., Werner, P., 2018. High-harmonic generation in Mott insulators. Phys. Rev. Lett. 121 (5), 057405.
- Nagaosa, N., Sinova, J., Onoda, S., MacDonald, A.H., Ong, N.P., 2010. Anomalous hall effect. Rev. Mod. Phys. 82 (2), 1539.
- Ndabashimiye, G., Ghimire, S., Wu, M., Browne, D.A., Schafer, K.J., Gaarde, M.B., Reis, D.A., 2016. Solid-state harmonics beyond the atomic limit. Nature 534 (7608), 520–523.
- Nishidome, H., Nagai, K., Uchida, K., Ichinose, Y., Yomogida, Y., Miyata, Y., Tanaka, K., Yanagi, K., 2020. Control of high-harmonic generation by tuning the electronic structure and carrier injection. Nano Lett. 20 (8), 6215–6221.
- Orlando, G., Ho, T.-S., Chu, S.-I., 2020. Simple model of dephasing for high-order harmonic generation in solids. JOSA B 37 (5), 1540–1549.

- Osika, E.N., Chacón, A., Ortmann, L., Suárez, N., Pérez-Hernández, J.A., Szafran, B., Ciappina, M.F., Sols, F., Landsman, A.S., Lewenstein, M., 2017. Wannier-Bloch approach to localization in high-harmonics generation in solids. Phys. Rev. X 7 (2), 021017.
- Pattanayak, A., Dixit, G., et al., 2020. Influence of vacancy defects in solid high-order harmonic generation. Phys. Rev. A 101 (1), 013404.
- Perelomov, A.M., Popov, V.S., Terent'ev, M.V., 1966. Ionization of atoms in an alternating electric field. Sov. Phys. JETP 50, 1393.
- Popmintchev, T., Chen, M.-C., Bahabad, A., Gerrity, M., Sidorenko, P., Cohen, O., Christov, I.P., Murnane, M.M., Kapteyn, H.C., 2009. Phase matching of high harmonic generation in the soft and hard X-ray regions of the spectrum. Proc. Natl. Acad. Sci. U. S. A 106 (26), 10516–10521.
- Price, H.M., Ozawa, T., Carusotto, I., 2014. Quantum mechanics with a momentum-space artificial magnetic field. Phys. Rev. Lett. 113 (19), 190403.
- Ralph, D.C., 2020. Berry curvature, semiclassical electron dynamics, and topological materials: lecture notes for introduction to solid state physics. arXiv preprint arXiv:2001.04797.
- Reiss, H.R., 1980. Effect of intense electromagnetic field on a weakly bound system. Phys. Rev. A 22, 1786.
- Resta, R., 1994. Macroscopic polarization in crystalline dielectrics: the geometric phase approach. Rev. Mod. Phys. 66 (3), 899.
- Resta, R., 2000. Manifestations of Berry's phase in molecules and condensed matter. J. Phys. Condens. Matter 12 (9), R107.
- Rossi, F., 1998. Bloch oscillations and Wannier-Stark localization in semiconductor superlattices. In: Theory of Transport Properties of Semiconductor Nanostructures, Springer, pp. 283–320.
- Rothhardt, J., Krebs, M., Hädrich, S., Demmler, S., Limpert, J., Tünnermann, A., 2014. Absorption-limited and phase-matched high harmonic generation in the tight focusing regime. New J. Phys. 16 (3), 033022.
- Saito, N., Xia, P., Lu, F., Kanai, T., Itatani, J., Ishii, N., 2017. Observation of selection rules for circularly polarized fields in high-harmonic generation from a crystalline solid. Optica 4 (11), 1333–1336.
- Schafer, K.J., Yang, B., DiMauro, L.F., Kulander, K.C., 1993. Above threshold ionization beyond the high harmonic cutoff. Phys. Rev. Lett. 70 (11), 1599.
- Schaibley, J.R., Yu, H., Clark, G., Rivera, P., Ross, J.S., Seyler, K.L., Yao, W., Xu, X., 2016. Valleytronics in 2D materials. Nat. Rev. Mater. 1 (11), 1–15.
- Schubert, O., Hohenleutner, M., Langer, F., Urbanek, B., Lange, C., Huttner, U., Golde, D., Meier, T., Kira, M., Koch, S.W., et al., 2014. Sub-cycle control of terahertz high-harmonic generation by dynamical Bloch oscillations. Nat. Photonics 8 (2), 119–123.
- Silva, R.E.F., Blinov, I.V., Rubtsov, A.N., Smirnova, O., Ivanov, M., 2018. High-harmonic spectroscopy of ultrafast many-body dynamics in strongly correlated systems. Nat. Photonics 12 (5), 266–270.
- Sivis, M., Taucer, M., Vampa, G., Johnston, K., Staudte, A., Naumov, A.Y., Villeneuve, D.M., Ropers, C., Corkum, P.B., 2017. Tailored semiconductors for high-harmonic optoelectronics. Science 357 (6348), 303–306.
- Sørngård, S.A., Simonsen, S.I., Hansen, J.P., 2013. High-order harmonic generation from graphene: strong attosecond pulses with arbitrary polarization. Phys. Rev. A 87 (5), 053803.
- Taguchi, Y., Oohara, Y., Yoshizawa, H., Nagaosa, N., Tokura, Y., 2001. Spin chirality, Berry phase, and anomalous hall effect in a frustrated ferromagnet. Science 291 (5513), 2573–2576.

- Tamaya, T., Ishikawa, A., Ogawa, T., Tanaka, K., 2016. Diabatic mechanisms of higher-order harmonic generation in solid-state materials under high-intensity electric fields. Phys. Rev. Lett. 116 (1), 016601.
- Tancogne-Dejean, N., Rubio, A., 2018. Atomic-like high-harmonic generation from two-dimensional materials. Sci. Adv. 4 (2), eaao5207.
- Tancogne-Dejean, N., Mücke, O.D., Kärtner, F.X., Rubio, A., 2017a. Ellipticity dependence of high-harmonic generation in solids originating from coupled intraband and interband dynamics. Nat. Commun. 8 (1), 1–10.
- Tancogne-Dejean, N., Mücke, O.D., Kärtner, F.X., Rubio, A., 2017b. Impact of the electronic band structure in high-harmonic generation spectra of solids. Phys. Rev. Lett. 118 (8), 087403.
- Tang, C.L., Rabin, H., 1971. Selection rules for circularly polarized waves in nonlinear optics. Phys. Rev. B 3 (12), 4025.
- Tani, M., Shinohara, Y., Sato, T., Ishikawa, K.L., 2020. Inter-atomic distance effects on high-harmonic generation by one-dimensional array. In: High Intensity Lasers and High Field Phenomena, Optical Society of America. HW6B–2.
- Taucer, M., Hammond, T.J., Corkum, P.B., Vampa, G., Couture, C., Thiré, N., Schmidt, B.E., Légaré, F., Selvi, H., Unsuree, N., et al., 2017. Nonperturbative harmonic generation in graphene from intense midinfrared pulsed light. Phys. Rev. B 96 (19), 195420.
- Thonhauser, T., Ceresoli, D., Vanderbilt, D., Resta, R., 2005. Orbital magnetization in periodic insulators. Phys. Rev. Lett. 95 (13), 137205.
- Vampa, G., Brabec, T., 2017. Merge of high harmonic generation from gases and solids and its implications for attosecond science. J. Phys. B At. Mol. Opt. Phys. 50 (8), 083001.
- Vampa, G., McDonald, C.R., Orlando, G., Klug, D.D., Corkum, P.B., Brabec, T., 2014. Theoretical analysis of high-harmonic generation in solids. Phys. Rev. Lett. 113 (7), 073901.
- Vampa, G., Hammond, T.J., Thiré, N., Schmidt, B.E., Légaré, F., McDonald, C.R., Brabec, T., Klug, D.D., Corkum, P.B., 2015a. All-optical reconstruction of crystal band structure. Phys. Rev. Lett. 115 (19), 193603.
- Vampa, G., Hammond, T.J., Thiré, N., Schmidt, B.E., Légaré, F., McDonald, C.R., Brabec, T., Corkum, P.B., 2015b. Linking high harmonics from gases and solids. Nature 522 (7557), 462–464.
- Vampa, G., McDonald, C., Fraser, A., Brabec, T., 2015c. High-harmonic generation in solids: bridging the gap between attosecond science and condensed matter physics. IEEE J. Sel. Top. Quantum Electron. 21 (5), 1–10.
- Vampa, G., McDonald, C.R., Orlando, G., Corkum, P.B., Brabec, T., 2015d. Semiclassical analysis of high harmonic generation in bulk crystals. Phys. Rev. B 91 (6), 064302.
- Vampa, G., Ghamsari, B.G., Mousavi, S.S., Hammond, T.J., Olivieri, A., Lisicka-Skrek, E., Naumov, A.Y., Villeneuve, D.M., Staudte, A., Berini, P., et al., 2017. Plasmon-enhanced high-harmonic generation from silicon. Nat. Phys. 13 (7), 659–662.
- Vampa, G., Lu, J., You, Y.S., Baykusheva, D.R., Wu, M., Liu, H., Schafer, K.J., Gaarde, M.B., Reis, D., Ghimire, S., 2020. Attosecond synchronization of extreme ultraviolet high harmonics from crystals. J. Phys. B At. Mol. Opt. Phys.
- Wang, C.-M., Ho, T.-S., Chu, S.-I., 2016. Determination of band structure from the intra-band power spectrum of high harmonic generation in crystal. J. Phys. B At. Mol. Opt. Phys. 49 (22), 225401.
- Wang, Z., Park, H., Lai, Y.H., Xu, J., Blaga, C.I., Yang, F., Agostini, P., DiMauro, L.F., 2017. The roles of photo-carrier doping and driving wavelength in high harmonic generation from a semiconductor. Nat. Commun. 8 (1), 1–7.
- Wilczek, F., Shapere, A., 1989. Geometric Phases in Physics. vol. 5 World Scientific.

- Wimmer, M., Price, H.M., Carusotto, I., Peschel, U., 2017. Experimental measurement of the Berry curvature from anomalous transport. Nat. Phys. 13 (6), 545–550.
- Wörner, H.J., Schild, A., Jelovina, D., Jordan, I., Perry, C., Luu, T.T., Yin, Z., 2020. Attosecond dynamics in liquids. arXiv preprint arXiv:2009.04913.
- Wu, M., Ghimire, S., Reis, D.A., Schafer, K.J., Gaarde, M.B., 2015. High-harmonic generation from Bloch electrons in solids. Phys. Rev. A 91 (4), 043839.
- Wu, M., Browne, D.A., Schafer, K.J., Gaarde, M.B., 2016. Multilevel perspective on high-order harmonic generation in solids. Phys. Rev. A 94 (6), 063403.
- Wu, M., You, Y., Ghimire, S., Reis, D.A., Browne, D.A., Schafer, K.J., Gaarde, M.B., 2017. Orientation dependence of temporal and spectral properties of high-order harmonics in solids. Phys. Rev. A 96 (6), 063412.
- Xiao, D., Shi, J., Niu, Q., 2005. Berry phase correction to electron density of states in solids. Phys. Rev. Lett. 95 (13), 137204.
- Xiao, D., Chang, M.-C., Niu, Q., 2010. Berry phase effects on electronic properties. Rev. Mod. Phys. 82 (3), 1959.
- Yoshikawa, N., Tamaya, T., Tanaka, K., 2017. High-harmonic generation in graphene enhanced by elliptically polarized light excitation. Science 356 (6339), 736–738.
- Yoshikawa, N., Nagai, K., Uchida, K., Takaguchi, Y., Sasaki, S., Miyata, Y., Tanaka, K., 2019. Interband resonant high-harmonic generation by valley polarized electron-hole pairs. Nat. Commun. 10 (1), 1–7.
- You, Y.S., Reis, D.A., Ghimire, S., 2017a. Anisotropic high-harmonic generation in bulk crystals. Nat. Phys. 13 (4), 345–349.
- You, Y.S., Wu, M., Yin, Y., Chew, A., Ren, X., Gholam-Mirzaei, S., Browne, D.A., Chini, M., Chang, Z., Schafer, K.J., et al., 2017b. Laser waveform control of extreme ultraviolet high harmonics from solids. Opt. Lett. 42 (9), 1816–1819.
- You, Y.S., Yin, Y., Wu, Y., Chew, A., Ren, X., Zhuang, F., Gholam-Mirzaei, S., Chini, M., Chang, Z., Ghimire, S., 2017c. High-harmonic generation in amorphous solids. Nat. Commun. 8 (1), 1–5.
- You, Y.S., Cunningham, E., Reis, D.A., Ghimire, S., 2018. Probing periodic potential of crystals via strong-field re-scattering. J. Phys. B At. Mol. Opt. Phys. 51 (11), 114002.
- Yu, C., Jiang, S., Wu, T., Yuan, G., Wang, Z., Jin, C., Lu, R., 2018. Two-dimensional imaging of energy bands from crystal orientation dependent higher-order harmonic spectra in h-BN. Phys. Rev. B 98 (8), 085439.
- Yu, C., Hansen, K.K., Madsen, L.B., 2019a. Enhanced high-order harmonic generation in donor-doped band-gap materials. Phys. Rev. A 99 (1), 013435.
- Yu, C., Jiang, S., Lu, R., 2019b. High order harmonic generation in solids: a review on recent numerical methods. Adv. Phys. X 4 (1), 1562982.
- Yu, C., Iravani, H., Madsen, L.B., 2020. Crystal-momentum-resolved contributions to multiple plateaus of high-order harmonic generation from bandgap materials. Phys. Rev. A 102 (3), 033105.
- Yue, L., Gaarde, M.B., 2020a. Imperfect recollisions in high-harmonic generation in solids. Phys. Rev. Lett. 124 (15), 153204.
- Yue, L., Gaarde, M.B., 2020b. Structure-and laser-gauges for the semiconductor Bloch equations in high-harmonic generation in solids. Phys. Rev. A 101, 053411.
- Zener, C., 1934. A theory of the electrical breakdown of solid dielectrics. Proc. R. Soc. Lond. A Containing Papers of a Mathematical and Physical Character 145 (855), 523–529.
- Zhang, G.P., Bai, Y.H., 2019. Magic high-order harmonics from a quasi-one-dimensional hexagonal solid. Phys. Rev. B 99 (9), 094313.
- Zhang, X., Li, J., Zhou, Z., Yue, S., Du, H., Fu, L., Luo, H.-G., 2019. Ellipticity dependence transition induced by dynamical Bloch oscillations. Phys. Rev. B 99 (1), 014304.

- Zhao, Y.-T., Jiang, S.-C., Zhao, X., Chen, J.-G., Yang, Y.-J., 2020. Effect of interband polarization on a solid's high-order-harmonic generation just below the band gap. Opt. Lett. 45 (10), 2874–2877.
- Zuo, R.-X., Song, X.-H., Liu, X.-W., Yang, S.-D., Yang, W.-F., 2019. Influence of intraband motion on the interband excitation and high harmonic generation. Chinese Phys. B 28 (9), 094208.
- Zurrón-Cifuentes, Ó., Boyero-García, R., Hernández-García, C., Picón, A., Plaja, L., 2019. Optical anisotropy of non-perturbative high-order harmonic generation in gapless graphene. Opt. Express 27 (5), 7776–7786.
- Zwiebach, B., 2018, Spring. 8.06 Quantum Physics III. https://ocw.mit.edu.